processes

MDPI

Article

Influence of External Store Distribution on the Flutter Characteristics of the Romanian IAR-99 HAWK Aircraft

Tudor Vladimirescu [1,2], Ion Fuiorea [2], Tudor Vladimirescu, Jr. [1] and Grigore Cican [2,3,*]

[1] Research Department, 3 Black Business Solutions Srl, Iancu de Hunedoara Blvd. No. 2, Bl. H6, Ap. 18, 011731 Bucharest, Romania; tudor.vladimirescu@gmail.com (T.V.)
[2] Faculty of Aerospace Engineering, National University of Science and Technology Politehnica Bucharest, 1-7 Polizu Street, 1, 011061 Bucharest, Romania
[3] National Research and Development Institute for Gas Turbines COMOTI, 220D Iuliu Maniu, 061126 Bucharest, Romania
* Correspondence: grigore.cican@upb.ro

Abstract

This study presents a flutter answer analysis of the Romanian IAR-99 HAWK advanced trainer aircraft equipped with multiple external store configurations. A high-fidelity finite element model (FEM) of the complete aircraft, including pylons and external stores, was coupled with a Doublet Lattice Method (DLM) aerodynamic model. The aeroelastic framework was validated against Ground Vibration Test (GVT) data to ensure structural accuracy. Four representative configurations were assessed: (A) RS-250 drop tanks on inboard pylons and PRN 16 × 57 unguided rocket launchers on outboard pylons; (B) four B-250 bombs; (C) eight B-100 bombs mounted on twin racks; and (D) a hybrid layout with B-100 bombs inboard and PRN 32 × 42 launchers outboard. Results show that spanwise distribution governs aeroelastic stability more strongly than total carried mass. Distributed stores lower wing-bending frequencies and densify the modal spectrum, producing critical pairs and subsonic crossings near M ≈ 0.82 at sea level, whereas compact heavy loads remain subsonic-stable. A launcher-specific modal family around ≈29.8 Hz is also identified in the hybrid layout. The validated FEM–DLM framework captures store-driven mode families (≈4–7 Hz) and provides actionable guidance for payload placement, certification, and modernization of the IAR-99 and similar platforms.

Keywords: flutter; aeroelasticity; FEM; IAR-99 aircraft; DLM method; external stores; flight safety

check for updates

Received: 2 September 2025
Revised: 19 September 2025
Accepted: 20 September 2025
Published: 25 September 2025

Citation: Vladimirescu, T.; Fuiorea, I.; Vladimirescu, T., Jr.; Cican, G. Influence of External Store Distribution on the Flutter Characteristics of the Romanian IAR-99 HAWK Aircraft. *Processes* **2025**, *13*, 3065. https://doi.org/10.3390/pr13103065

Copyright: © 2025 by the authors. Licensee MDPI, Basel, Switzerland. This article is an open access article distributed under the terms and conditions of the Creative Commons Attribution (CC BY) license (https://creativecommons.org/licenses/by/4.0/).

1. Introduction

Aeroelasticity represents a critical interdisciplinary field that addresses the interaction between aerodynamic forces, inertial effects, and structural elasticity. Among the various aeroelastic phenomena, flutter is the most dangerous because it can lead to rapidly divergent oscillations and catastrophic structural failure if not adequately controlled [1]. As such, flutter analysis is a mandatory requirement in the design, development, and certification of both civil and military aircraft [2]. International certification standards such as MIL-A-8870 and EASA CS-23/25 explicitly require that aircraft be free from flutter and other dynamic instabilities across the entire operational flight envelope, with sufficient safety margins above the design dive speed [3,4].

Several studies in aeroelastic literature highlight the diversity and criticality of flutter problems across different aircraft configurations and mission profiles. Ref. [5] analyzed

the flutter behavior of subsonic wings using a reduced-order structural model based on Euler–Bernoulli beam theory combined with unsteady aerodynamic loads. Their results demonstrated how both bending and torsional flexibility can strongly affect the critical speed, showing that even relatively simple structural modifications may alter flutter margins significantly. Similarly, Ref. [6] investigated flutter instabilities in flying-wing configurations through the NASA X-56A research program. They emphasized the phenomenon of Body Freedom Flutter (BFF), where low-frequency rigid-body modes couple with wing flexibility, producing instabilities at speeds much lower than those predicted by classical approaches. This study underscored the importance of accurately representing global elastic–inertial couplings in aeroelastic models.

The role of control surfaces has also been studied extensively. Ref. [7] investigated the flutter of flexible wings with deformable flaps, combining experimental and numerical methods. They demonstrated that localized flexibility in control surfaces may create additional dynamic couplings with wing bending and torsion, reducing flutter speed and introducing new instability mechanisms. Their findings are particularly relevant for military trainer and combat aircraft, where multiple movable surfaces are integrated into lightweight structures.

Nonlinear aeroelastic phenomena have also been addressed. Ref. [8] examined high-aspect-ratio wings carrying external ballast masses, revealing that nonlinear interactions can lead to limit cycle oscillations (LCO), even before classical flutter onset. Their analysis confirmed that store-induced oscillations at frequencies around 5–10 Hz may couple with wing modes and substantially lower the effective aeroelastic safety margins. This highlights the necessity of considering both linear flutter predictions and nonlinear dynamic responses when assessing the stability of aircraft carrying external stores [9].

Complementary to these studies, advanced numerical methods have been developed to capture the complex interaction between structures and unsteady aerodynamics. Ref. [10] proposed a hybrid FEM–DLM and CFD-based reduced-order modeling approach to predict the aeroelastic response of wing–store systems. Their methodology proved efficient in capturing interference effects between the wing, pylons, and suspended stores, achieving good agreement with experimental benchmarks. Such approaches demonstrate the robustness and adaptability of FEM–DLM techniques in modern aeroelastic analysis, especially for configurations involving external stores.

Recent advances in flutter research have focused on both methodological developments and practical applications with external stores. Ref. [11] introduced CFD-based techniques for flutter prediction through the generation of generalized aerodynamic forces, combining reduced-order models with high-fidelity CFD solvers to capture nonlinear aeroelastic behavior at significantly lower computational cost. Recent research on flying-wing UAVs has shown that Body Freedom Flutter (BFF) depends strongly on stiffness and mass distribution. Two main modes were identified—plunge-dominant and pitch-dominant—and the flutter speed is highest near the transition between them. Designing structural properties close to this transition can improve stability margins, offering valuable guidance for UAV aeroelastic design [12].

Complementary work [13] on a 2.5D C/SiC composite blade under wake excitation highlighted the critical role of material damping and anisotropy in flutter onset, providing insights that are transferable to aircraft wing–store interactions.

With respect to external load effects, Ref. [14] conducted a flight safety analysis of military aircraft with heavy external stores, concluding that inappropriate pylon placement or asymmetric loading may severely compromise flutter margins.

An experimental investigation has recently examined the effect of dual external stores mounted beneath the wing of a generic subsonic light aircraft. Tests conducted in the

UTM Low Speed Wind Tunnel compared clean, single-store, and dual-store configurations, revealing that external stores significantly modify aerodynamic performance and stability. The results showed a reduction in lift coefficient by up to 13% and a decrease in longitudinal static stability, while rolling stability was improved and directional stability remained largely unaffected. Additionally, flow visualization indicated that external stores delayed flow separation to higher angles of attack, underscoring their complex influence on aerodynamic and stability characteristics [15].

Recent advances have also explored active suppression techniques, where an H∞ control algorithm applied to a wing–store system demonstrated that feedback control using piezoelectric actuators can effectively mitigate store-induced instabilities and increase flutter speed [16].

Recent developments have also introduced data-driven approaches, where deep learning algorithms applied to F-18 flutter flight test signals proved effective in identifying critical parameters with short data sequences, thus reducing the risks associated with prolonged exposure near the flutter boundary [17].

Recent investigations have highlighted that the combined influence of structural damage and external stores can have a critical impact on transonic flutter stability. Using the Transonic Small Disturbance (TSD) method, it was shown that, while subsonic flutter margins remain relatively unaffected, in the transonic regime even moderate levels of structural damage to control surface supporting elements, when coupled with external store installation, may drastically reduce stability limits. These findings underline the importance of explicitly accounting for both structural integrity and store-induced effects when assessing aeroelastic safety in fighter-type aircraft [18] while Ref. [19] showed that active vibration control strategies can effectively restore stability in a wing–store system.

In modern fighter and transport aircraft, underwing external stores are often required when fuselage space is limited, but their installation can significantly modify aerodynamic performance. Wind tunnel experiments on a generic subsonic fighter showed that store placement near the wingtip and at one-third span from the root increased the lift coefficient up to 1.09, while flaperon deflections improved efficiency at moderate angles of attack (10–12°) but also introduced higher drag at larger angles, highlighting the trade-offs between lift enhancement and stability [20].

In Ref. [21], a novel approach is developed for flutter stability under hybrid uncertainties (random and epistemic). Their framework provided stochastic stability margins and demonstrated its effectiveness through reference cases. Ref. [22] introduced a refined aeroelastic beam finite element to study the stability of flexible lifting structures in subsonic regimes, focusing on efficient structural–aerodynamic coupling for flutter prediction.

Ref. [23] investigated the effects of external stores mounted spanwise on the aeroelastic response and flutter of straight and swept wings, showing the sensitivity of critical flutter speed to store mass and position; Ref. [24] modeled a free aircraft wing with external stores in roll maneuver using Theodorsen + Galerkin. Numerical results, validated experimentally, revealed that flutter boundaries are highly sensitive to angular roll velocity, fuselage mass, and store mass/position; and Ref. [25] presented a flutter analysis of the KF-16 fighter equipped with new ECM pods (ALQ). Using GVT modal data directly in MSC.NASTRAN 2012®, they demonstrated a methodology for flight envelope clearing, enabling safe operation with external stores.

Taken together, these investigations confirm that the integration of external stores—such as fuel tanks, bombs, or rocket launchers—introduces new aeroelastic challenges. The added mass and inertia, together with aerodynamic interference effects, systematically reduce flutter margins and may trigger coupling phenomena between store oscillations and structural modes [26,27].

The importance of flutter prediction and suppression becomes even more pronounced in aircraft equipped with external stores, such as fuel tanks, bombs, or rocket launchers. These elements, while essential for mission versatility, introduce significant structural and aerodynamic modifications. The addition of external stores increases the overall mass and inertia of the aircraft, alters the load distribution across the wing and fuselage, and shifts the natural frequencies of the structure. Furthermore, stores are often suspended on pylons, forming complex store–pylon–wing systems that can introduce new oscillatory modes. These modes may couple with the primary bending or torsional modes of the wing, resulting in a reduction of the flutter margin. Consequently, the aeroelastic stability of aircraft carrying external stores must be carefully evaluated during certification, as neglecting these effects could compromise flight safety [28].

Despite the significant progress in flutter research, most of the studies reported in the literature focus either on isolated wing models, flying-wing UAVs, or high-performance fighter and transport aircraft. By contrast, comprehensive aeroelastic investigations of complete trainer aircraft configurations are scarce, particularly when considering the combined effects of pylons and multiple external stores. Light military trainers such as the IAR-99 are widely used for both pilot instruction and tactical missions, often carrying various underwing payloads that can critically alter their aeroelastic stability. However, to date there is a clear gap in published studies addressing the flutter behavior of trainer aircraft in multiple external store configurations. This motivates the present work, which develops and validates an FEM–DLM based aeroelastic methodology for the IAR-99, providing a systematic flutter analysis across four representative store arrangements in order to support safe certification and enhance the aircraft's operational performance.

2. Materials and Methods

The aim of the present study is to develop and validate a robust FEM–DLM aeroelastic methodology applied to the flutter analysis of the IAR-99 HAWK. The methodology incorporates a high-fidelity finite element model of the entire aircraft, including pylons and external stores, and an aerodynamic model based on the Doublet Lattice Method, which accounts for interference between all relevant lifting and non-lifting surfaces. Modal analyses are validated against Ground Vibration Test (GVT) data to ensure structural accuracy. Flutter predictions are then carried out for both clean and external store configurations using the p–k method, with results evaluated against established certification criteria. By doing so, this work provides a comprehensive evaluation of the IAR-99's flutter margins and introduces a validated methodology that can be extended to other training and light combat aircraft.

2.1. IAR-99 HAWK Aircraft Descriptions

The IAR-99 HAWK is a Romanian subsonic jet trainer, developed by Avioane Craiova (Craiova, Romania) under the coordination of INCAS specialists, intended for both advanced pilot training and light combat missions. Conceived in the 1980s as a cost-effective alternative to supersonic fighters, the aircraft was designed in a dual-control (DC) version for training, with the possibility of conversion into a single-control (SC) variant to extend operational capabilities and reduce costs [29].

Structurally, the IAR-99 features a conventional aerodynamic configuration with a trapezoidal low-wing layout, swept tail surfaces and retractable tricycle landing gear. The airframe is primarily of all-metal semi-monocoque construction, designed to withstand intensive training use while ensuring robust flight characteristics. The tandem cockpit, equipped with modern avionics and ejection seats, enables both instructional and operational roles.

The baseline variant is powered by a Rolls-Royce Viper 632-41 turbojet, providing maximum thrust of around 18 kN at ISA sea level conditions and enabling speeds of approximately 850–865 km/h with a service ceiling of about 12,900 m. Through modernization programs, remotorized versions (e.g., with the Viper 680-43) demonstrated improved performance, including higher climb rates, increased range (up to 1590 km), and reduced take-off and landing distances. A detailed description can be found in Refs. [30,31].

The transition from DC to SC configuration allowed installation of additional fuel tanks in the space freed by the second cockpit, thus extending endurance and tactical radius. In its upgraded versions, the IAR-99 Șoim was also fitted with advanced avionics and weapons systems, enabling missions similar to those of supersonic fighters in the subsonic domain, except for high-altitude interception.

By combining relatively low acquisition and operating costs with versatile performance and avionics compliant with NATO requirements, the IAR-99 HAWK remains a relevant example of an advanced subsonic trainer, suitable for integration into combat pilot training programs while reducing reliance on more expensive supersonic aircraft. Its structural and aeroelastic characteristics make it a valuable case study for flutter investigations.

An overview of the single-control IAR-99 HAWK aircraft is presented in Figure 1.

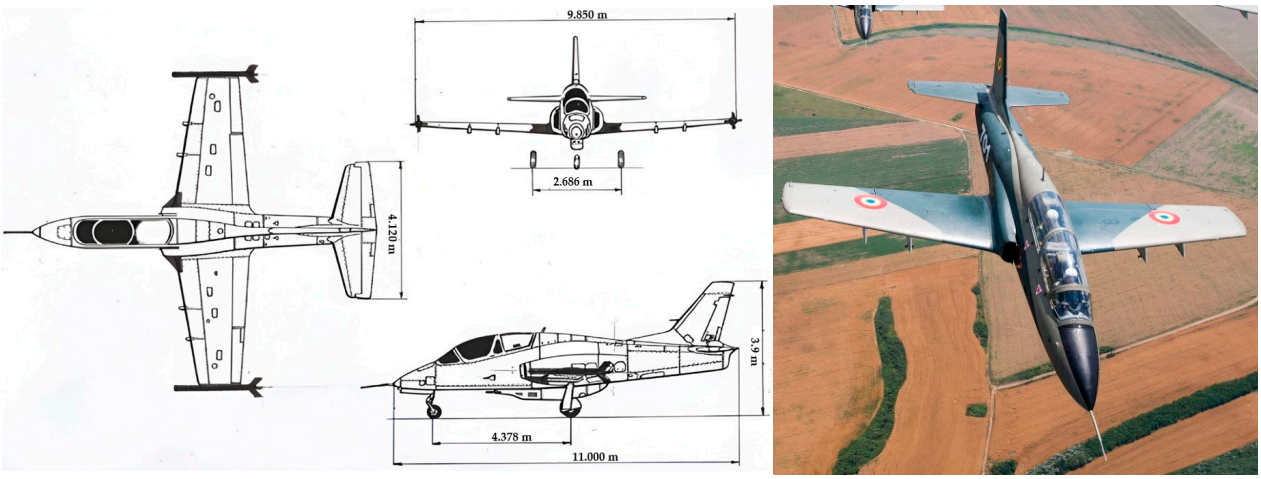


Figure 1. Plan view of the SC advanced trainer IAR-99 HAWK.

2.2. FEM Structural Model in Clean Configuration

The finite element model of the IAR-99 HAWK in clean configuration was developed to capture the structural behavior of the main components: the wing, fuselage, empennages, and external hardpoints (when attached in later stages). The wing is of trapezoidal planform with an integral torsion box and fuel tanks in each panel, modeled with classical elements and combined structures for flaps and ailerons. The fuselage was represented as a semi-monocoque construction, divided into the forward, central, and aft sections, each joined by bolts and fittings. The central fuselage was modeled with special attention to the wing–fuselage junction and to the hardpoints for the centerline store. The horizontal stabilizer has a trapezoidal configuration with a conventional structure, while the elevators use a mixed metallic and sandwich structure. The vertical stabilizer was modeled as a trapezoidal fin with a classic framework, the rudder having a combined metallic-sandwich layout.

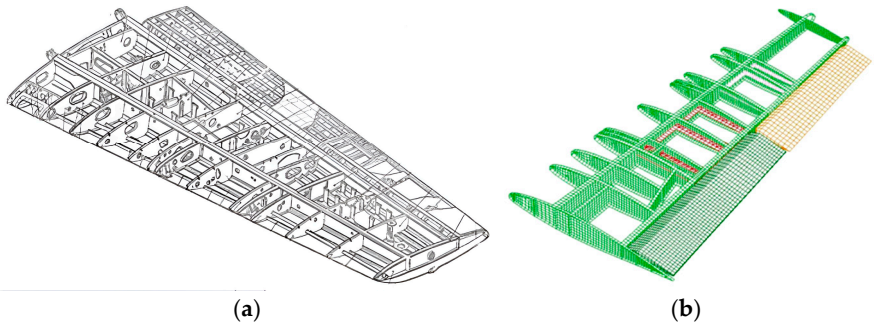
The material properties were defined according to the real structure: aluminum alloys 2024T3-T2 and 6065 ($E = 73.1 \times 10^3$ MPa, $\rho \approx 2.72–2.79 \times 10^{-3}$ g/mm^3), high-strength steels ($E = 200–207 \times 10^3$ MPa, $\rho \approx 6.6–7.86 \times 10^{-3}$ g/mm^3), and Plexiglas acrylic for canopy components ($E = 2.76–3.3 \times 10^3$ MPa, $\rho \approx 1.18–1.19 \times 10^{-3}$ g/mm^3).

The model was built in MSC.NASTRAN®, using standardized elements (CQUAD4, CTRIA3, CROD, etc.). The global FEM mesh included over 565,000 nodes and 584,000 elements, with the structural skin represented by more than 240,000 shell elements. The wing structure was represented by approximately 24,572 nodes and 76,582 elements, with the discretization dominated by CQUAD4 elements (76,408) and a small number of triangular CTRIA3 elements (174), sufficient to capture the trapezoidal geometry and torsional stiffness of the wing box. The rear fuselage included about 72,340 nodes and 64,164 elements, again modeled mainly with quadrilateral shells (62,570 CQUAD4) complemented by 1594 triangular elements. The central fuselage, which represents the junction zone with the wing and centerline store attachment, was discretized with 74,776 nodes and 35,092 elements, of which 64,018 are quadrilaterals and 2282 triangles, reflecting the need for higher mesh density in load transfer areas. The posterior fuselage together with the empennages accounted for the largest share of the model, with over 337,484 nodes and 167,448 elements, including more than 113,652 quadrilateral elements, capturing the interaction of the fin, stabilizers, and tail fuselage. Finally, the skin was meshed independently with 56,379 nodes and 241,508 elements, where quadrilaterals (241,982) were complemented by 22,114 triangles, allowing a refined representation of aerodynamic surfaces and local stiffness distribution.

Overall, the global FEM contained 565,551 nodes and 584,794 elements, of which 558,630 were quadrilateral (CQUAD4) and 26,164 triangular (CTRIA3), providing a robust balance between computational efficiency and accuracy. This detailed discretization ensured that the model had sufficient degrees of freedom to reproduce both the global elastic behavior and the local stress concentrations required for aeroelastic and flutter analyses.

Boundary conditions reflected the free-flight state of the aircraft, with rigid-body modes verified to ensure model consistency. Concentrated masses (equipment, fuel, systems) were distributed according to Annexes of the structural data. The resulting FEM model provided a high number of degrees of freedom, enabling detailed analysis of global and local deformations, aeroelastic coupling, and the foundation for flutter simulations.

In the following Figures 2–7, the FEM is shown without the external skins for clarity, and both the real structural assemblies and their corresponding finite element meshes are illustrated. This comparative presentation emphasizes how the physical geometry was transferred into the numerical model for aeroelastic analysis.



(**a**) (**b**)

Figure 2. Wing structure (**a**) and FEM model (**b**).

The real wing has a trapezoidal planform with an integral torsion box, fuel tanks and control surfaces (flaps and ailerons). The FEM mesh uses predominantly quadrilateral shell elements, refined in the wing root area to capture torsional loads and wing–fuselage interactions.

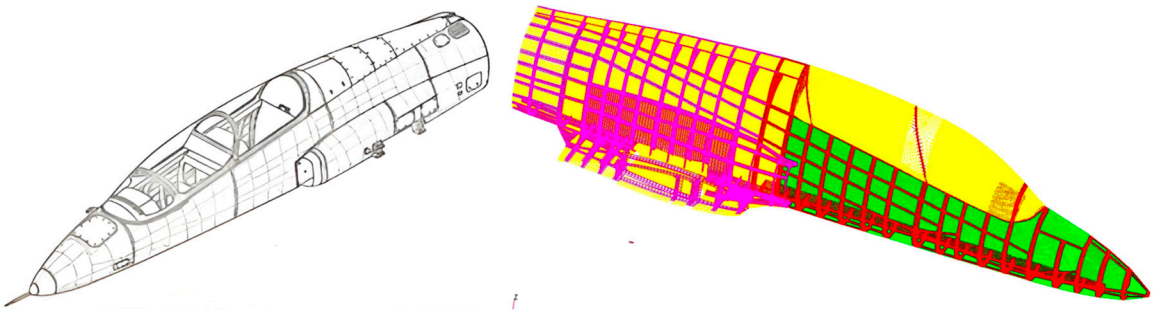


Figure 3. Main fuselage assembly and FEM model.

The fuselage is built as a semi-monocoque metallic structure with frames and longerons ensuring rigidity. In the FEM model, the skin is meshed with regular quadrilaterals, while higher density elements are placed near cut-outs and reinforcement zones. The real structure shows the load-carrying frames and stiffened panels. In the FEM representation, shell elements reproduce the skin while beam elements model the internal structure, ensuring accurate stiffness and load transfer. The forward fuselage includes the cockpit and nose section. The FEM mesh is finer around the canopy and avionics bay, where geometric discontinuities increase stress concentrations. The canopy consists of metallic frames and Plexiglas panels. Its mesh combines shell and solid elements, with denser discretization in curved areas to reproduce transparency panels and load transfer through the frame.

The real nose assembly integrates the cockpit, avionics bay, and windshield. The mesh reflects high refinement around attachment points and transparent surfaces. The central fuselage houses the air intake and engine mounts. The FEM discretization is refined around intake lips and wing–fuselage fittings to accurately model aerodynamic and structural loads.

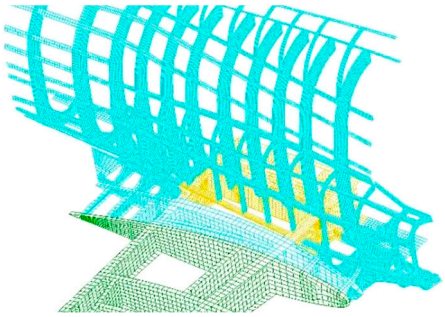


Figure 4. Wing–fuselage junction FEM mesh.

The real junction is reinforced with fittings to transfer loads. The FEM mesh uses a high density of quadrilaterals and triangles in this critical zone to ensure realistic stiffness.

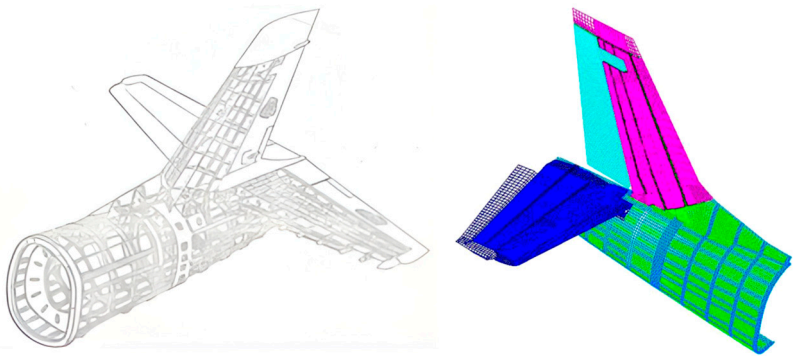


Figure 5. Rear fuselage structure and FEM model.

The aft fuselage is made of riveted metallic panels with frames. The mesh follows the structural lines, with uniform quadrilaterals on the skin. The assembly integrates the rear fuselage with the tailplane and vertical fin. The FEM discretization is denser at the attachment points of the horizontal and vertical stabilizers.

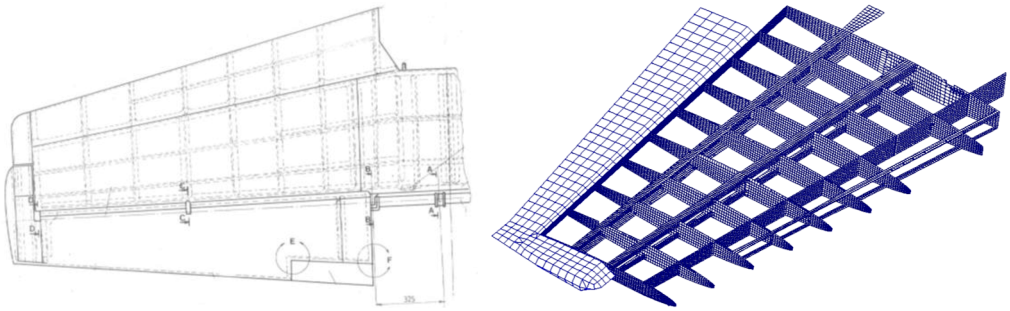


Figure 6. Horizontal tailplane structure and FEM model.

The real stabilizer has a trapezoidal planform with an elevator. The mesh is arranged along spars and ribs, with refinement at hinge and attachment zones. The discretization emphasizes the root area where bending loads are highest. The elevator is meshed separately to reproduce its flexibility and control surface motion.

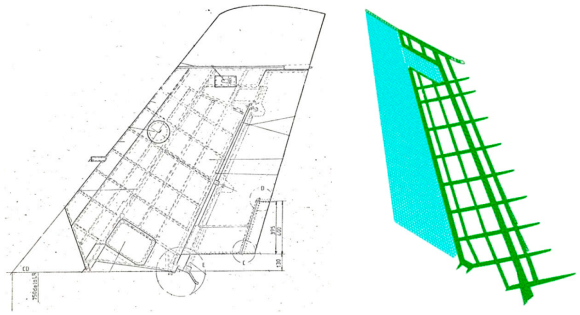


Figure 7. Structure of the vertical tailplane and FEM model.

There is a trapezoidal fin with a conventional structure and a rudder featuring a combined layout (conventional + metallic sandwich). The corresponding FEM mesh uses mainly shell elements, with local refinement at the fin root (junction with the fuselage) and along the rudder hinge line to capture bending and torsional modes. The discretization predominantly employs CQUAD4 elements, with CTRIA3 used only in curvature/joint regions. Local mesh refinement is placed around attachments and at the fin base to accurately model local stiffness and the interaction with the fuselage.

The structural model was verified under free–free boundary conditions to ensure the presence of the six rigid-body modes, and a WEIGHTCHECK audit (mass/C.G./inertia) was carried out to screen for inconsistencies in materials and element properties. The modal basis retained for aeroelastic coupling includes the fundamental elastic modes of wing and empennages as well as control surface modes.

The result of the weight check is presented in Chart 1. The first box on the left highlights a 3 $\times$ 3 matrix that shows the model's mass on the main diagonal. These values are repeated in the second box in the table, and unless table items with some atypical properties are present, with different masses in different directions, the three values should all be the same. The box on lines 4–6 and columns 4–6, respectively, shows the inertia properties of the model in relation to the reference point. The matrices in the boxes between lines 4–6 and columns 1–3, respectively, and lines 1–3 and columns 4–6, are used in the calculation of the center of gravity (C.G.) in relation to a reference point. By

default, this point is the origin of the basic coordinate system in MSC.NASTRAN®. The three columns labeled X-C.G., Y-C.G., and Z-C.G. provide the coordinates of the model's center of mass calculated around the corresponding axis values. Note that zeros are given for the corresponding axes in columns X-C.G., Y-C.G., and Z-C.G.

```
    O U T P U T   F R O M   G R I D   P O I N T   W E I G H T   G E N E R A T O R
                                REFERENCE POINT =        0
                                      M O
*  4.532521E+00  0.000000E+00  0.000000E+00  0.000000E+00 -1.576609E+02 -1.111014E+02 *
*  0.000000E+00  4.532521E+00  0.000000E+00  1.576609E+02  0.000000E+00  3.464115E+04 *
*  0.000000E+00  0.000000E+00  4.532521E+00  1.111014E+02 -3.464115E+04  0.000000E+00 *
*  0.000000E+00  1.576609E+02  1.111014E+02  1.173041E+07 -1.179309E+06 -2.092011E+05 *
* -1.576609E+02  0.000000E+00 -3.464115E+04 -1.179309E+06  2.839809E+08 -3.027559E+04 *
* -1.111014E+02  3.464115E+04  0.000000E+00 -2.092011E+05 -3.027559E+04  2.943766E+08 *
                                      S
                    *  1.000000E+00  0.000000E+00  0.000000E+00 *
                    *  0.000000E+00  1.000000E+00  0.000000E+00 *
                    *  0.000000E+00  0.000000E+00  1.000000E+00 *
          DIRECTION
    MASS AXIS SYSTEM (S)     MASS              X-C.G.       Y-C.G.       Z-C.G.
           X              4.532521E+00     0.000000E+00  2.451204E+01 -3.478437E+01
           Y              4.532521E+00     7.642800E+03  0.000000E+00 -3.478437E+01
           Z              4.532521E+00     7.642800E+03  2.451204E+01  0.000000E+00
                                      I(S)
                    *  1.172220E+07  3.301833E+05  1.414172E+06 *
                    *  3.301833E+05  1.922008E+07  3.414018E+04 *
                    *  1.414172E+06  3.414018E+04  2.961850E+07 *
                                      I(Q)
                    *  1.923452E+07                             *
                    *                2.972957E+07               *
                    *                             1.159669E+07 *
                                       Q
                    *  4.341590E-02  7.825811E-02  9.959873E-01 *
                    * -9.990536E-01  7.783883E-04  4.348841E-02 *
                    *  2.628056E-03 -9.969328E-01  7.821784E-02 *
```

Chart 1. Using WEIGHTCHECK to show mass, C.G. location and inertia properties.

Without atypical properties, it is expected, as is shown in the table, that two of the values in each column are identical, providing a component of the location C.G. The three matrices at the bottom of this output provide the values of the moments of inertia with respect to the C.G. and the main axes. This result must be evaluated in relation to all known information about the actual structure. Is the mass obtained in accordance with the known data for the actual structure? Do different sets produce the same mass? Is C.G.'s location reasonable? A careful analysis of these values can often reveal erroneous material and/or property records in the proposed FEM model.

It should be noted that the values for mass are given in tons and the dimensions are given in mm. Since we have applied three unitary inertial loads, we can also check whether the net force on the structure is equal to the mass multiplied by the acceleration.

2.3. Aerodynamic Modeling (DLM)

2.3.1. Brief Methodological Frame

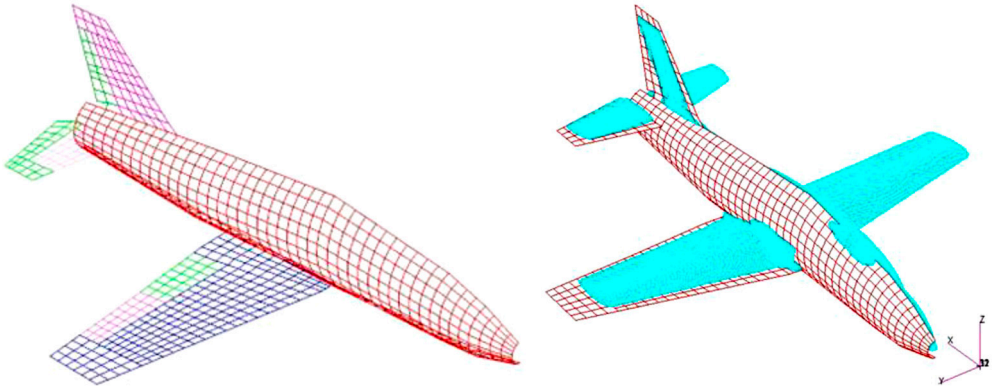
For the computation of unsteady aerodynamic forces in subsonic flow, we used the Doublet Lattice Method (DLM) in the frequency domain. Lifting surfaces are partitioned into trapezoidal panels; the no-penetration condition is enforced at the three-quarter-chord control points, yielding influence matrices that form the generalized aerodynamic forces Q(k,M) later used in the flutter solution. In the implementation adopted here, bodies (fuselage, and later pylon/store) are represented by thin-body plus interference elements to capture local shielding and wake effects.

2.3.2. Application to the IAR-99 in Clean Configuration

All aerodynamic surfaces and bodies considered (wing, horizontal/vertical tail, fuselage) were assigned penalizations/interference-body definitions. Inputs for lifting surfaces are chord and span; for thin-bodies (fuselage), the inputs are length and thickness dis-

tributions. The coverage rule specified that lifting surfaces and thin-bodies must fully cover the geometry used in the aircraft's FEM structural model to ensure a consistent aeroelastic coupling.

In the following Figures 8–12, the aerodynamic idealization is overlaid on the validated structural mesh to demonstrate geometric coverage and the alignment of aerodynamic control points with structural load paths (spars, longerons, frames). This ensures that the DLM lifting surface panels and thin-body/interference elements fully cover the FEM model prior to aeroelastic assembly.



(**a**) (**b**)

Figure 8. DLM methodology for the clean configuration (**a**) and DLM over FEM—complete aircraft (**b**).

The workflow schematic for the subsonic DLM setup was as follows: paneling of wing and tailplanes, thin-body/interference representation of the fuselage, coverage checks, and coupling to the p-k flutter solution via the generalized aerodynamic force matrix Q(k,M). There was a global overlay confirming full coverage of lifting surfaces and fuselage by DLM elements; aerodynamic control points lie over structurally meaningful regions to secure consistent load transfer in coupling.

After presenting the overlay for the complete aircraft, additional DLM over FEM overlays are included for the main components to provide further detail. These views confirm local geometric coverage, correct placement of control points, and mesh refinement in regions with high structural and aerodynamic gradients, ensuring a coherent aeroelastic coupling for the flutter analysis.

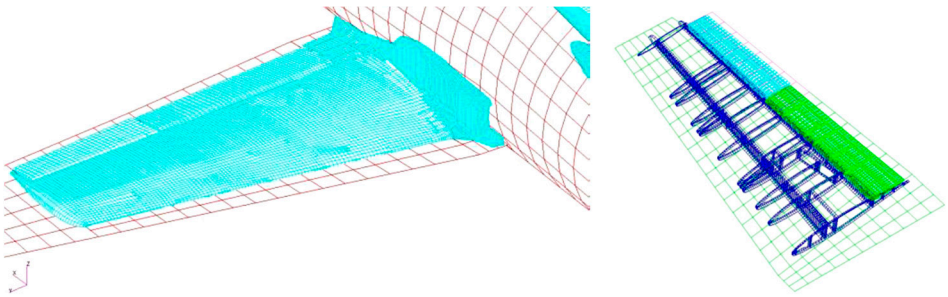


Figure 9. DLM over FEM—wing.

The trapezoidal wing is panelized in chord and span; panel density is increased toward the root and along high-gradient zones to capture torsional stiffness and wing–fuselage interactions. Control points are at 0.75 c, consistent with the DLM formulation.

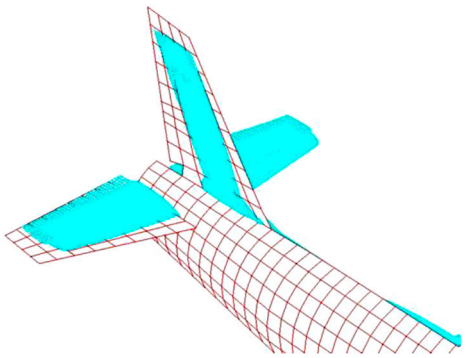
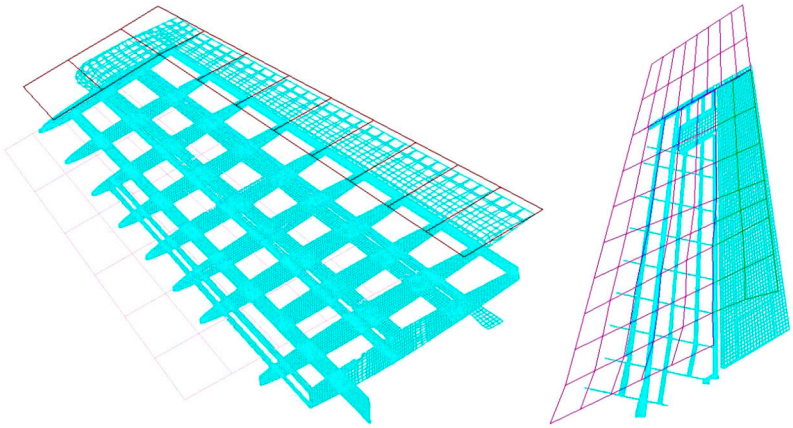


Figure 10. DLM over FEM—empennages and aft fuselage.

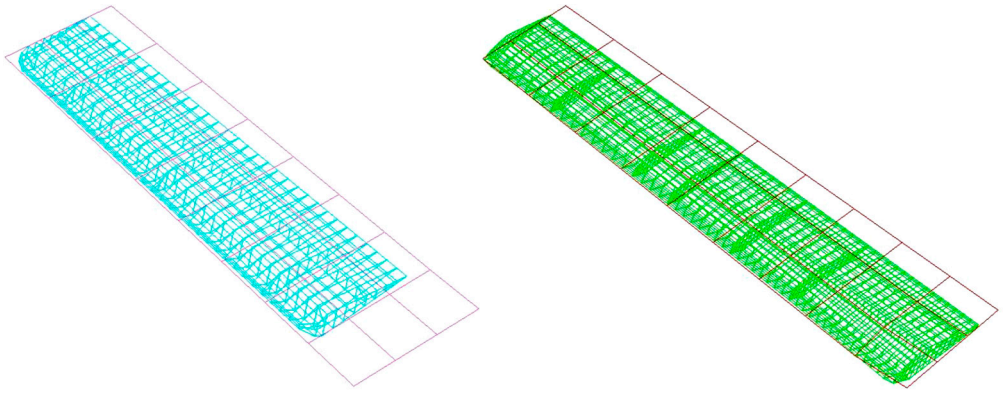
There is overlay of horizontal/vertical tails together with the aft fuselage: refined paneling at tailplane roots; thin-body/interference elements along the aft fuselage model shielding and local wake effects near the tails.



(**a**) (**b**)

Figure 11. DLM over FEM—horizontal tailplane (**a**) and vertical tailplane (**b**).

There is chordwise/spanwise paneling of the stabilizer; refinement along the root attachment and elevator hinge line represent bending/torsion and control surface kinematics in the aeroelastic model. There is paneling of the fin with local densification near the fin root (junction with the fuselage) and along the rudder hinge line, while interference elements capture the proximity effects with the aft fuselage.



(**a**) (**b**)

Figure 12. DLM over FEM—aileron (**a**) and flap (**b**).

There is a Local lifting surface patch (and/or extra aerodynamic points) along the aileron span with refined paneling at the hinge; the overlay shows how aileron motion is

introduced in the aerodynamic grid and transferred into the wing panels. There is refined paneling around the flap hinge and side edges to capture local unsteady loads; the overlay confirms correct geometric coverage to support the control surface contribution in the generalized forces.

The computational framework is entirely based on a frequency-domain aeroelastic formulation, where generalized aerodynamic forces are obtained using the Doublet Lattice Method (DLM) and coupled with the finite element model through the p–k method. In this approach, the structural modes are introduced directly in the frequency domain, and the flutter boundary is identified by tracking the damping variation of coupled aeroelastic modes as a function of flight speed. No transformation of time histories into spectra was performed, and no power spectral density analysis was required. Instead, the analysis follows the classical and widely accepted aeroelastic workflow in which the DLM provides unsteady aerodynamic influence coefficients in the Laplace domain, later interpolated in frequency to construct the aeroelastic system matrices. This procedure has been extensively documented and validated in the aeroelastic literature, and its robustness has been confirmed by numerous parametric and sensitivity studies [32,33]. By emphasizing the direct frequency-domain formulation, we ensure both methodological clarity and consistency with established practices in the field of computational aeroelasticity.

2.4. Representative External Store Configurations-FEM

A set of four representative configurations was selected to cover a broad spectrum of structure–store interactions and wing mass distributions. Taken together, the four configurations (A–D) range from fuel plus unguided rocket combinations to heavy symmetric loads with 250-kg bombs and multiple light-bomb layouts, providing a consistent basis for assessing mass and inertia effects and W/F/P/S aerodynamic coupling in the computation of Q(k,M) and in the p-k flutter solution reported in Section 3. To faithfully document the integration of external stores into the model, we present below visual descriptions of the components (RS-250, B-250, B-50, B-100, PRN 16 × 57, PRN 32 × 42) together with their corresponding FEM models. Accordingly, Figure 13 shows the inboard and outboard pylons to which the stores or bombs used in all four configurations are attached.

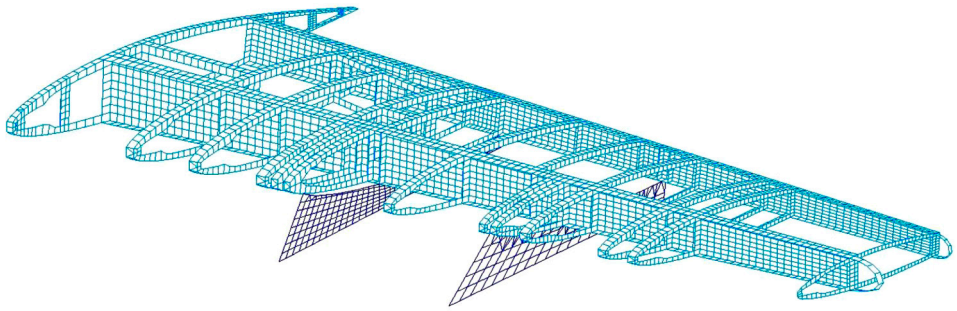
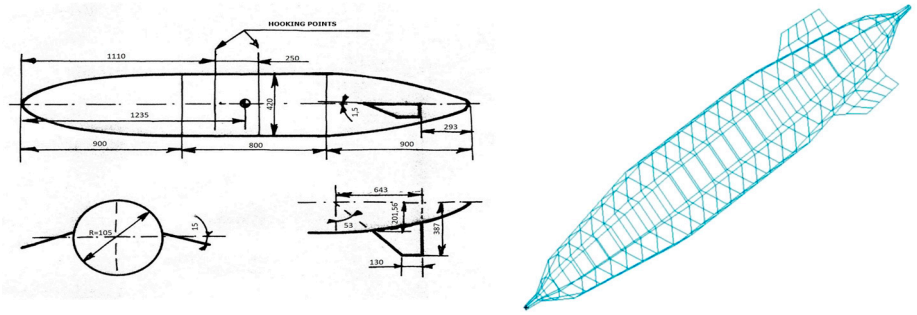


Figure 13. FEM model—wing detail with mounting pylons.

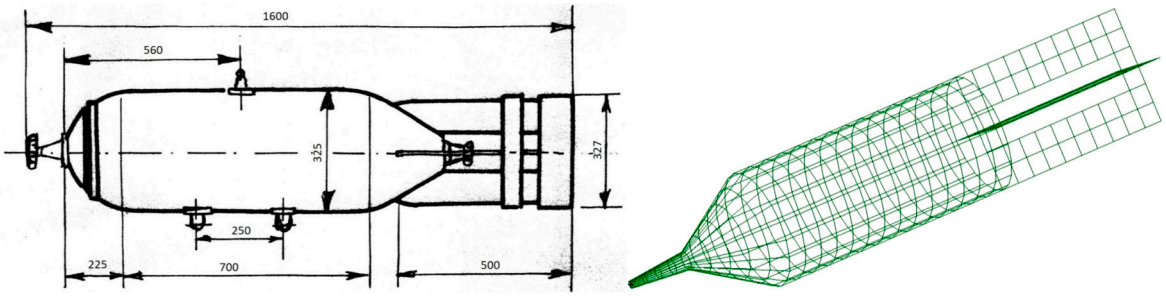
Local FEM discretization at the pylon stations is shown. The skin, spars, and ribs are meshed mainly with quadrilateral shells, with local refinement at the pylon pads, fastener lines, and rib–spar intersections; a few triangles appear near fairing curvature. Pylons are shell-modeled and constrained to the wing, capturing stiffness jumps and load transfer needed for aeroelastic (flutter) analysis. Figure 14 presents the RS-250 external fuel tank—mounted view and dimensions (a), and the FEM model (b).



(**a**) (**b**)

Figure 14. RS-250 external fuel tank—mounted view and dimensions (**a**), and FEM model (**b**).

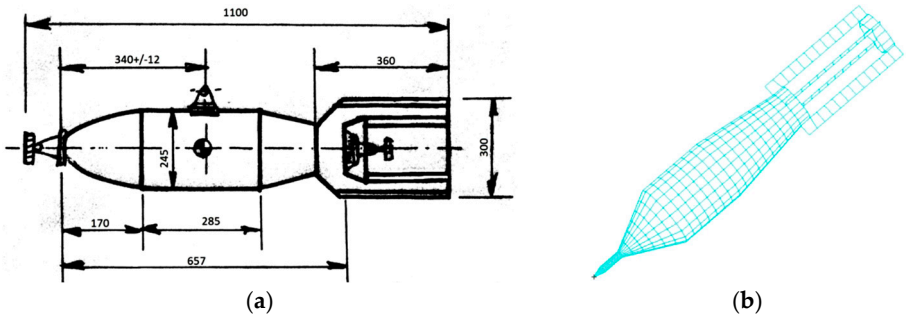
The RS-250 has an axisymmetric ogive–cylindrical–ogive shape; the drawing shows mounting-point spacing and key diameters for placement on the inboard pylon. The FEM model uses shell elements aligned along meridians and hoops, with local refinement at the nose/tail tapers and around the attachment lugs to capture curvature and stiffness jumps. This discretization preserves the tank's bending/torsion response and mass distribution, ensuring reliable load transfer to the wing and consistent aeroelastic coupling later. Figure 15 presents the B-250 external fuel tank—mounted view and dimensions (a), and the FEM model (b).



(**a**) (**b**)

Figure 15. B-250 aerial bomb—mounted view and dimensions (**a**), and FEM model (**b**).

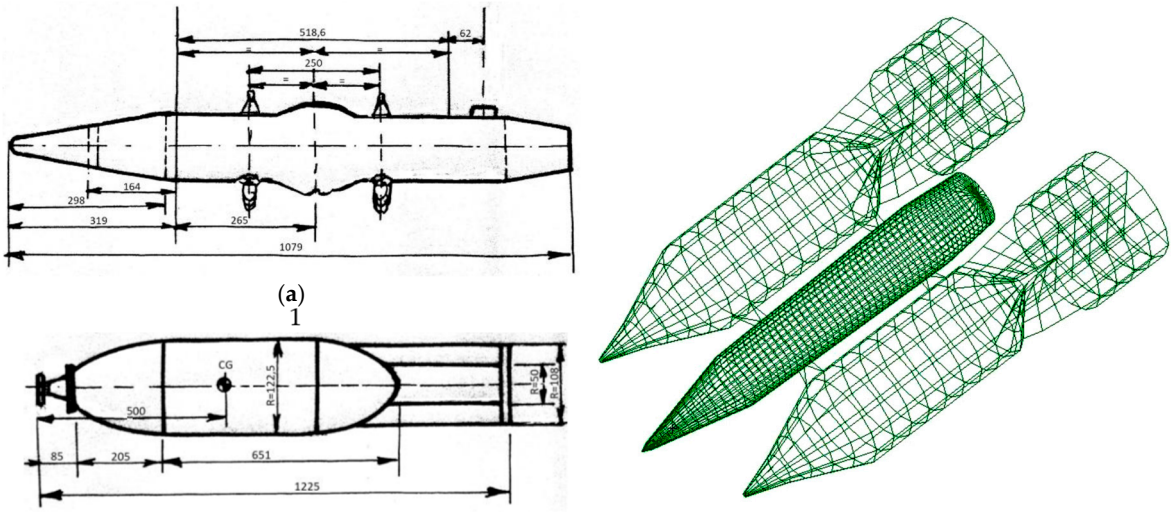
The B-250 has an ogive nose, cylindrical mid-body, and tapered tail section; the drawing indicates overall length, body diameter, and the spacing of the suspension lugs for pylon attachment. The FEM idealization uses shell elements arranged along meridians and hoops, with local refinement at the nose/tail transitions and around the lug area to capture curvature and stiffness jumps. The tail section is further refined to represent the slender cone and stabilizing fittings, ensuring realistic mass/stiffness distribution and load transfer into the pylon–wing system for aeroelastic analysis. Figure 16 presents the B-50 external fuel tank—mounted view and dimensions (a), and the FEM model (b).



(**a**) (**b**)

Figure 16. B-50 high-explosive aerial bomb—mounted view and dimensions (**a**), FEM model (**b**).

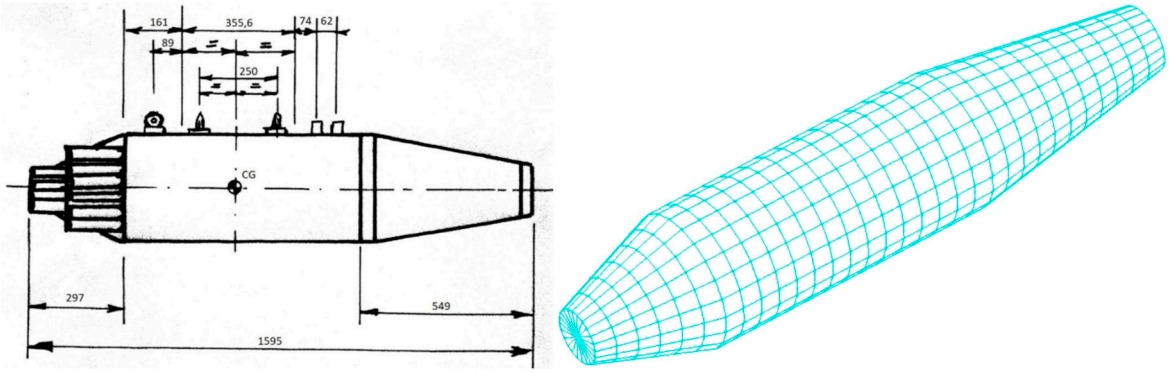
The B-50 features a rounded-ogive nose, a short cylindrical mid-body, and a tapered aft section with a finned tail unit; the drawing specifies overall length, body diameter, and lug positions for mounting. The FEM idealization uses shell elements arranged along meridians/hoops, with local refinement at the nose–shoulder and tail transitions, around the suspension lugs, and within the tail box/fin region. This captures curvature and stiffness jumps, preserving realistic mass–stiffness distribution and load transfer into the pylon–wing system for aeroelastic analysis. Figure 17 presents the Twin rack for 2× B-100 (a), B-100 bomb (b), and FEM model of the twin-rack assembly with 2× B-100 (c).



(**a**) (**b**) (**c**)

Figure 17. Twin rack for 2× B-100 (**a**), B-100 bomb (**b**), and FEM model of the twin-rack assembly with 2× B-100 (**c**).

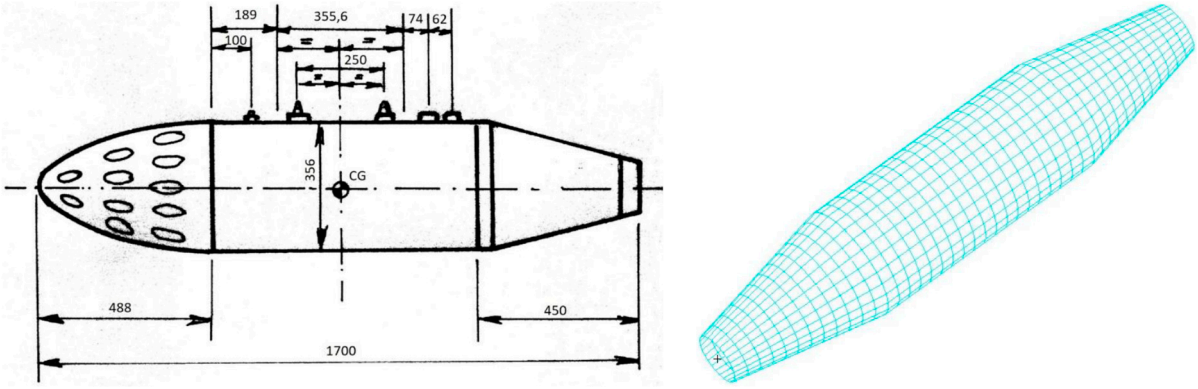
The twin rack carries two B-100 bombs; the drawings indicate overall length, lug spacing, and the B-100 C.G. for proper pylon placement. In the FEM assembly, the rack and each bomb are meshed with shell elements; refinement is applied at the rack adapters/sway-brace pads and around the bomb suspension lugs, as well as along the nose–tail tapers to capture curvature. The bombs are tied to the rack through constrained interface nodes (no free edges), preserving realistic mass–stiffness distribution and load transfer to the pylon. This discretization also enables the model to capture rack–store interaction and potential multi-store coupling in the aeroelastic analysis. Figure 18 presents the PRN 15 × 57 rocket launcher block—mounted view and dimensions (a), and FEM model (b).



(**a**) (**b**)

Figure 18. PRN 15 × 57 rocket launcher block—mounted view and dimensions (**a**), and FEM model (**b**).

The PRN 15 × 57 launcher has a cylindrical main body with a tapered nose and a frontal cluster of tube mouths; the drawing provides overall length, C.G. location, and lug spacing for pylon attachment. The FEM idealization models the launcher as a thin-walled shell aligned along meridians/hoops, with local refinement at the nose/shoulder transitions and around the suspension lugs. Additional densification is applied near the tube-mouth face to capture stiffness jumps, ensuring realistic mass–stiffness distribution and load transfer to the pylon for subsequent aeroelastic analysis. Figure 19 presents the PRN 32 × 42 rocket launcher block—mounted view and dimensions (a), and FEM model (b).



(**a**) (**b**)

Figure 19. PRN 32 × 42 rocket launcher block—mounted view and dimensions (**a**), and FEM model (**b**).

The PRN 32 × 42 launcher features an ogive nose with multiple outlet apertures, a cylindrical mid-body, and a short tapered aft section; the drawing indicates overall length, C.G. position, and suspension lug spacing for pylon mounting. The FEM idealization uses thin-shell elements laid out along meridians and hoops, with local refinement around the perforated nose face, at shoulder transitions, and in the lug region to capture curvature and stiffness jumps. This discretization preserves a realistic mass–stiffness distribution and ensures credible load transfer to the pylon for downstream aeroelastic (flutter) analysis.

Configuration A is a mixed training/operational layout, with RS-250 drop tanks on the inboard pylons and PRN 16 × 57 rocket launchers on the outboard pylons, introducing moderate concentrated masses and local aerodynamic interference near the wing. Structurally, relative to the clean model (565,551 nodes/584,794 elements), this configuration adds +528 nodes/+504 elements for the two tanks and +1456 nodes/+1498 elements for the two launchers, yielding a total of 567,535 nodes and 586,796 elements (+0.35% nodes; +0.34% elements). The number of CTRIA3 elements increases from 26,164 to 26,258 (+94), and CQUAD4 from 558,630 to 560,538 (+1908), essentially preserving the same share of quadrilaterals in the mesh (~95.4% of the total), which supports numerical stability and accurate local stiffnesses. Mesh refinement is concentrated at the attachment regions (wing pads and suspension lugs), at shape transitions (ogive/shoulder), and at spar–rib intersections, to capture stiffness jumps and load transfer from the store into the wing box. This discretization level is then used for the aeroelastic coupling (DLM–FEM) and the p-k flutter solution (Figure 20).

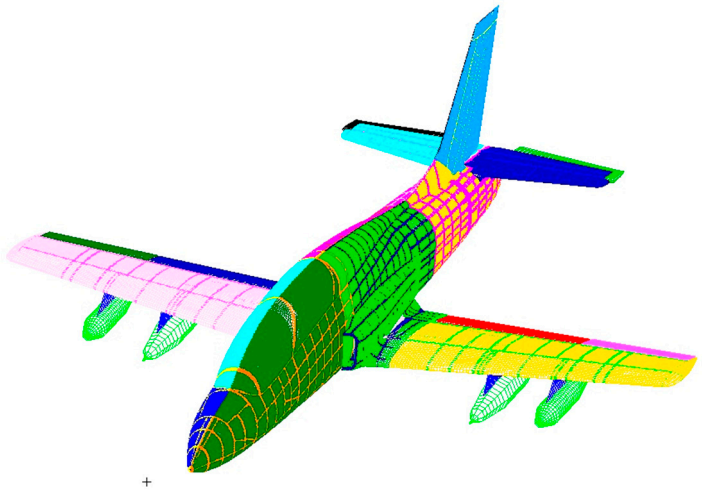


Figure 20. IAR-99 in Configuration A—FEM model.

Configuration B represents the heavy, symmetric case, with four B-250 bombs installed on the inboard and outboard pylons of each semi-span, producing a marked increase in total mass/inertias and a stronger coupling with the wing-bending modes. Structurally, relative to the clean model (565,551 nodes/584,794 elements), the 4× B-250 adds +2888 nodes (+0.51%) and +2192 elements (+0.38%), for a total of 568,439 nodes and 586,986 elements. The increase appears exclusively in CQUAD4 (+2192, from 558,630 to 560,822), while CTRIA3 remains unchanged (26,164), thus keeping the quadrilateral share at ~95.6% and supporting numerical stability. Mesh refinement is concentrated at the suspension lugs and shape transitions (nose/shoulder, finned tail) to capture stiffness jumps and the load transfer from the bombs into the pylon–wing system. This discretization is then used for DLM–FEM coupling and the p-k flutter solution (Figure 21).

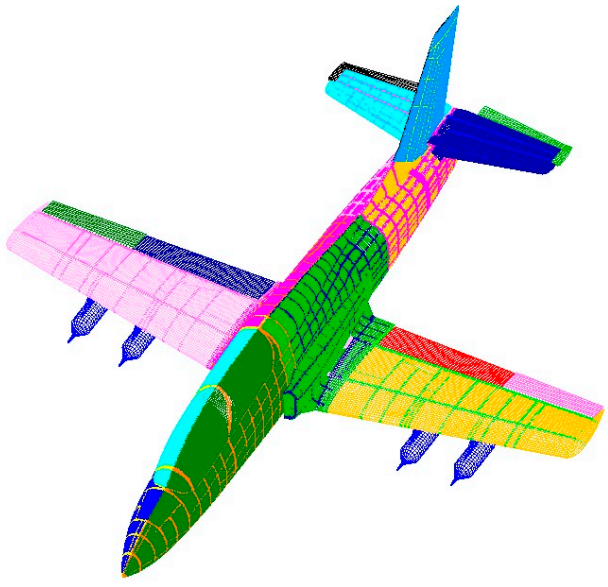


Figure 21. IAR-99 in Configuration B—FEM model.

Configuration C explores a "multi-site" distribution of lighter stores: four twin racks, each carrying 2× B-100 (eight B-100 in total, one twin rack on each inboard and outboard pylon). This layout is useful for assessing vibration coupling among multiple stores with nearby natural frequencies. Structurally, relative to the clean model (565,551 nodes/584,794 elements), the multi-rack payload adds +10,868 nodes (+1.92%) and +10,438 elements (+1.78%), for totals of 576,419 nodes and 595,232 elements. The

increase splits into +304 CTRIA3 and +10,132 CQUAD4, keeping quadrilaterals at about 95.55% of the mesh (568,764/595,232), which preserves numerical stability and accurate local stiffness. Refinement is concentrated at rack adapters and sway-brace pads, around bomb suspension lugs, and along the nose–tail tapers, to capture stiffness jumps and load transfer paths (Figure 22).

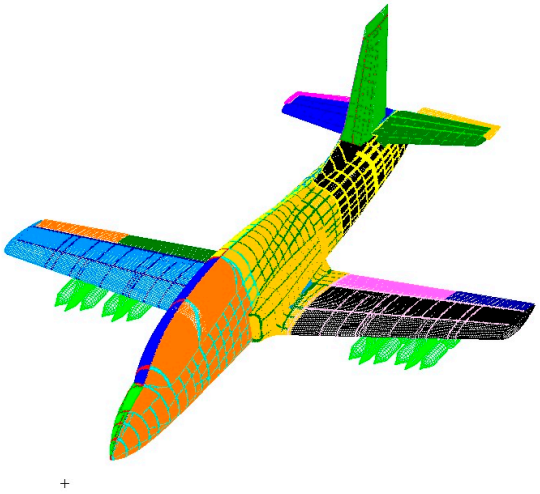


Figure 22. IAR-99 in Configuration C—FEM model.

Configuration D is a mixed layout designed to induce different aerodynamic interference at the inboard vs. outboard stations: twin racks with 2× B-100 on the inboard pylons and PRN 32 × 42 rocket launchers on the outboard pylons (left–right symmetric). This combination is useful to probe flutter sensitivity when "bomb-like" bodies and launcher-type interference tubes coexist on the same semi-span. Structurally, relative to the clean model (565,551 nodes/584,794 elements), the payload adds +5434 nodes/+5218 elements for the two B-100 racks and +2464 nodes/+2408 elements for the two launchers, yielding 573,449 nodes and 592,420 elements overall (+1.40% nodes; +1.30% elements). CTRIA3 increases from 26,164 to 26,316 (+152), and CQUAD4 from 558,630 to 566,104 (+7474), keeping quadrilaterals at ~95.6% of the mesh—supportive of numerical stability and accurate local stiffness. Mesh refinement is concentrated at suspension lugs, rack adapters/sway-brace pads, and at nose/shoulder transitions on both store types to capture stiffness jumps and load transfer paths into the pylon–wing system (Figure 23).

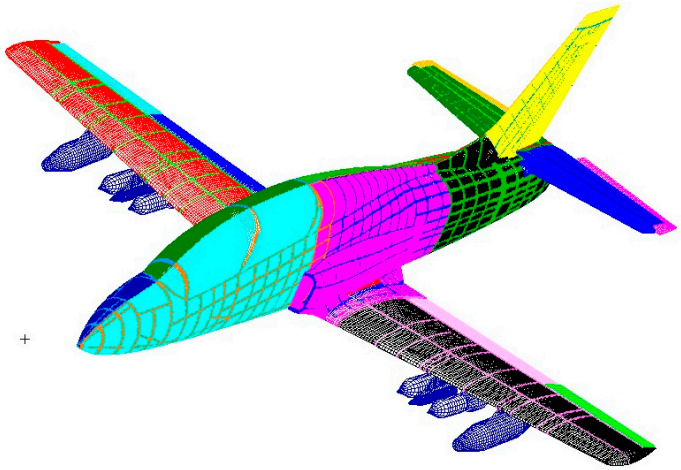


Figure 23. IAR-99 in Configuration D—FEM model.

2.5. Application to the IAR-99 in A–D Configuration

This subsection documents how the aerodynamic model (DLM) was extended from the clean aircraft to four representative store configurations (A–D) and overlaid on the validated FEM mesh to ensure full geometric coverage and consistent aeroelastic coupling. For each configuration, we generated DLM over FEM overlays at aircraft level and, where needed, at component level (wing, empennages, pylons, and stores). These overlays verify that (i) lifting surface panels and thin-/interference-body elements completely "dress" the structural geometry, (ii) control points lie over structurally meaningful load paths (spars/longerons/frames), and (iii) store bodies are grouped with proximate lifting surfaces within W/F/P/S interference groups (wing/fuselage/pylon/store).

In the following Figure 24, the aerodynamic idealization is overlaid on the validated structural mesh to demonstrate geometric coverage and the alignment of aerodynamic control points with structural load paths (spars, longerons, frames).

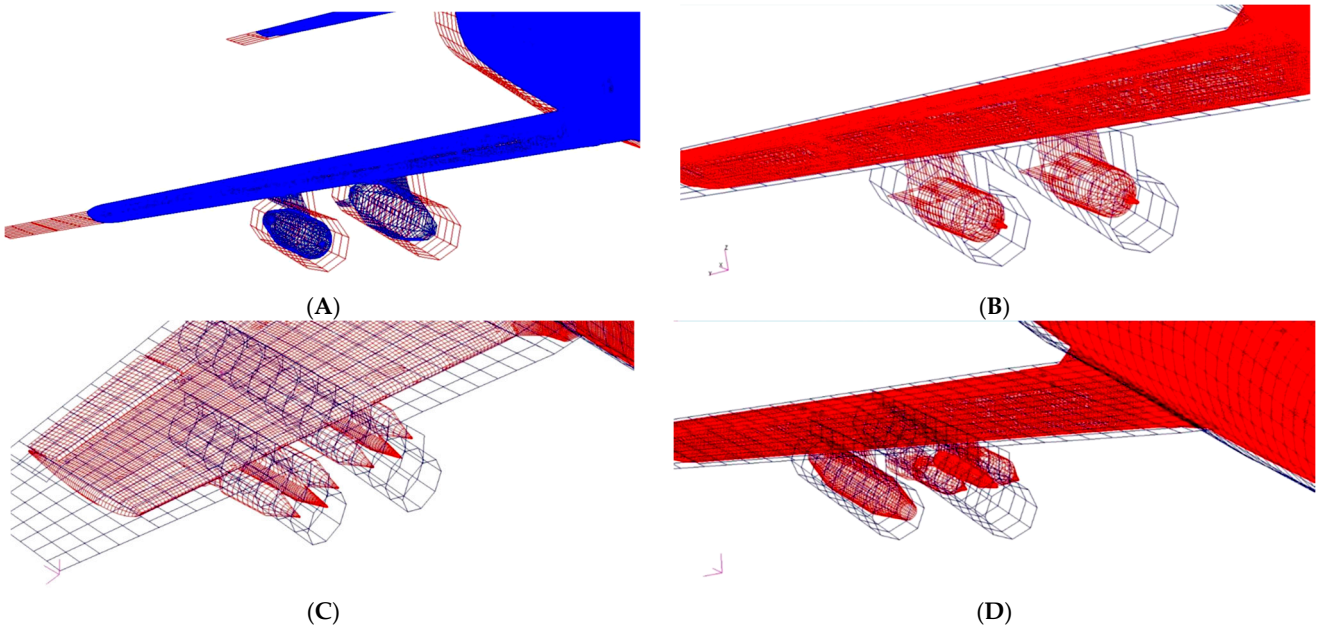


Figure 24. DLM over FEM for the 4 configurations.

For all four external store configurations, the DLM over FEM overlays confirm full geometric coverage, correct placement of aerodynamic control points, and consistent grouping of thin-body/interference elements with nearby lifting panels (W/F/P/S), ensuring credible aeroelastic coupling. In Configuration A, aircraft- and component-level overlays show local panel refinement around pylon pads. In Configuration B, denser paneling appears near suspension lugs and nose/shoulder transitions, with bombs attached to the intersected wing panels via interference tubes. In Configuration C, overlays highlight refined paneling at each rack station and proper attachment of store tubes to the wing, isolating near-field rack–bomb–wing interactions. In Configuration D, overlays validate coverage for both store types and their per-semi-span grouping; panel densification is evident at rack pads and the perforated launcher faces, so aerodynamic control points coincide with key stiffness jumps for reliable modal coupling.

3. Results

Before presenting the aeroelastic results, the adequacy of the finite element discretization was verified. To ensure the robustness of the model, a mesh convergence verification was performed. The analysis was initiated with a coarse mesh, which was progressively refined in regions of high stress and modal deformation gradients (e.g., wing root, control

surface hinge lines, and pylon–store interfaces). The primary modal frequencies of interest (first bending and torsional modes) were monitored at each refinement step. The results showed that two consecutive refinement levels produced nearly identical modal frequencies, with differences below 1%, while the corresponding mode shapes exhibited a modal assurance criterion (MAC) higher than 0.98. This indicates that the numerical solution is not significantly affected by further refinement and that the selected mesh density provides reliable results at reasonable computational cost. Such an iterative mesh-refinement process is a standard practice in aeroelastic finite element modeling and has been similarly applied in recent studies [34,35].

3.1. Result for Clean Aircraft Configuration

3.1.1. Modal Characteristics (Clean FEM)

Using the validated FEM and the Lanczos eigensolver, the free-vibration analysis of the clean IAR-99 model confirms the six rigid-body modes at near-zero frequencies: roll f = 0.000801896 Hz, yaw 0.001479020 Hz, vertical translation along OZ 0.001877410 Hz, lateral translation along OY 0.001995730 Hz, longitudinal translation along OX 0.002120370 Hz, and pitch 0.002748500 Hz. The first elastic mode is the symmetric flap rotation at 11.6789 Hz, followed closely by an antisymmetric aileron rotation at 11.6920 Hz. Next come the bending modes: symmetric wing bending at 16.4099 Hz and vertical tail bending at 18.2297 Hz. The aileron family continues with an antisymmetric aileron rotation at 19.4495 Hz, and a coupled mode of wing bending with symmetric aileron rotation at 21.6891 Hz. At higher frequencies, the horizontal tail and elevator modes appear: antisymmetric horizontal tail bending at 37.2379 Hz, symmetric elevator rotation at 40.1101 Hz, antisymmetric elevator rotation at 43.1151 Hz, and another symmetric elevator rotation at 47.5907 Hz. This modal hierarchy will be used as the coupling basis for the aeroelastic calculations and for interpreting the figures that follow.

The sequence in Figures 25–30 shows the six rigid-body modes of the clean IAR-99 model—roll, yaw, vertical, lateral, longitudinal translations, and pitch—appearing at near-zero frequencies ($\approx 10^{-3}$ Hz). This confirms that the model was analyzed in free–free conditions and satisfies standard quality criteria for aeroelastic use: all rigid-body frequencies were well below ~0.01 Hz and there was a large separation between the sixth rigid-body mode and the first elastic mode ($\gg 1/100$). In parallel, a mass/C.G./inertia audit (WEIGHTCHECK) verifies the consistency of total mass, center of gravity location, and principal inertias, ruling out spurious constraints or property errors before coupling.

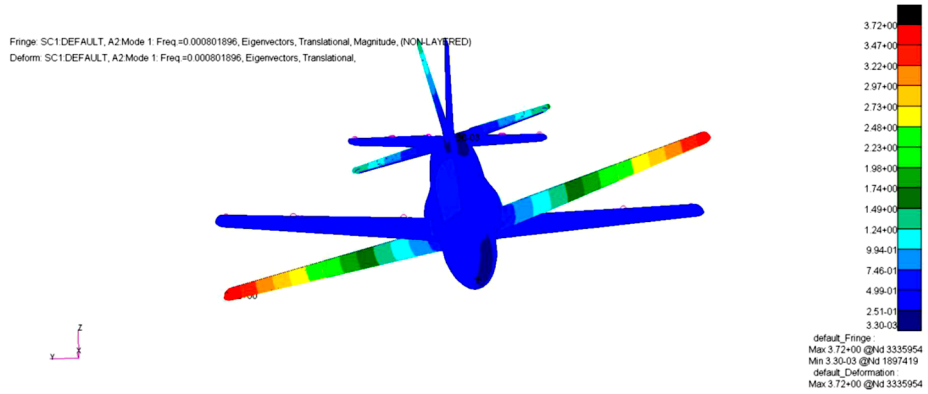


Figure 25. Rigid-body mode—Roll: f = 0.000801896 Hz.

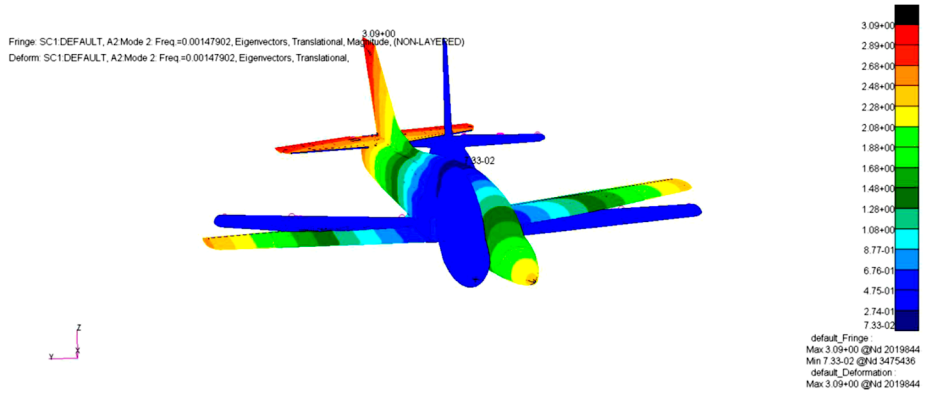


Figure 26. Rigid-body mode—Yaw: f = 0.001479020 Hz.

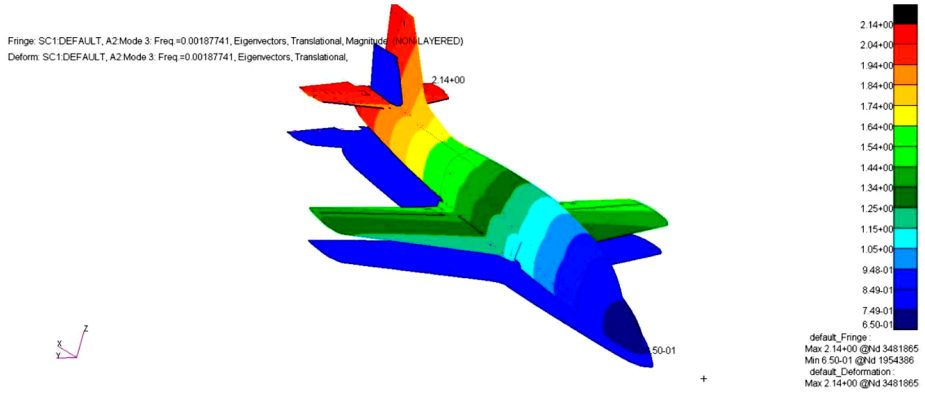


Figure 27. Rigid-body mode—Vertical translation along OZ: f = 0.001877410 Hz.

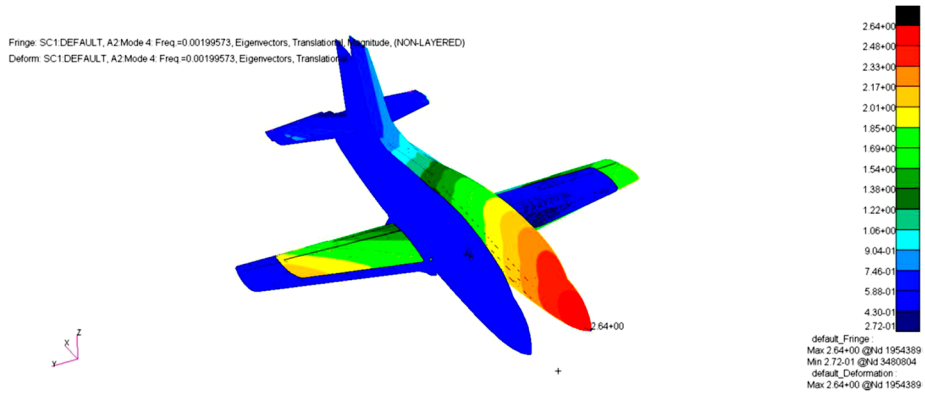


Figure 28. Rigid-body mode—Lateral translation along OY: f = 0.001995730 Hz.

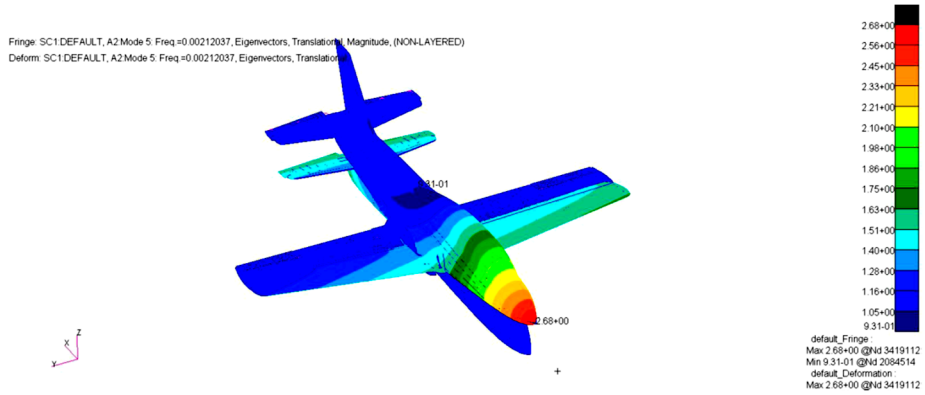


Figure 29. Rigid-body mode—Longitudinal translation along OX: f = 0.002120370 Hz.

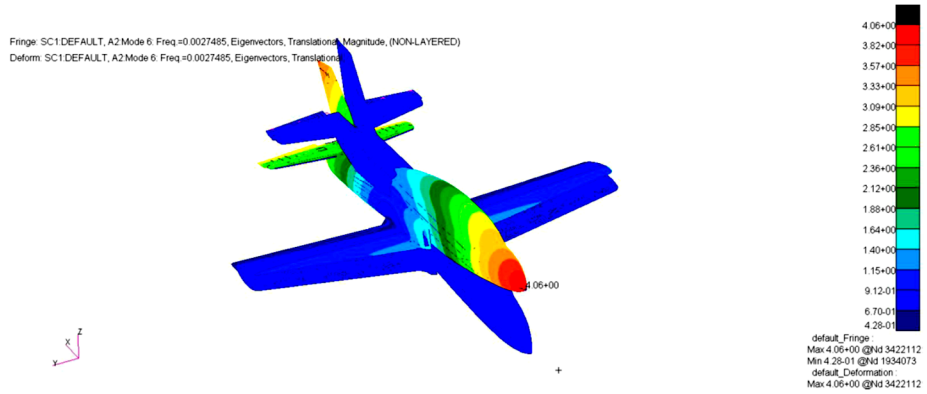


Figure 30. Rigid-body mode—Pitch: f = 0.002748500 Hz.

Figures 31 and 32 introduce the first elastic family on the control surfaces: a symmetric flap rotation at 11.6789 Hz followed closely by an antisymmetric flap rotation at 11.6924 Hz, a pairing that reflects the local flap–wing coupling and establishes the lower bound of the elastic spectrum used for aeroelastic assembly.

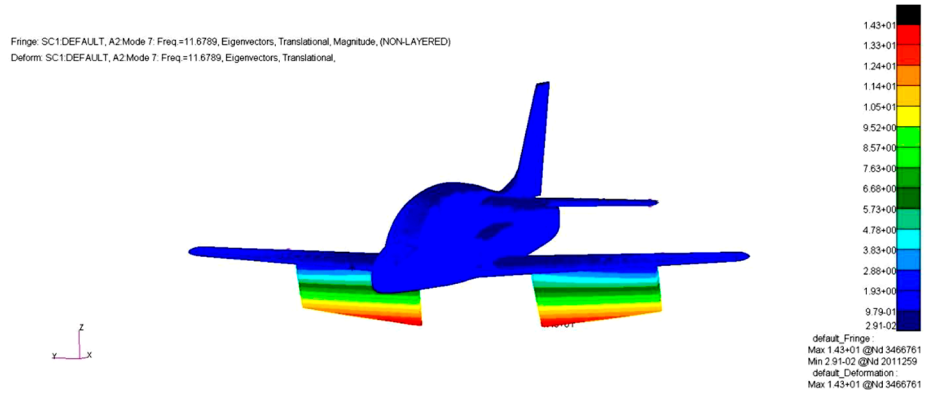


Figure 31. Symmetric flap rotation mode: f = 11.6789 Hz.

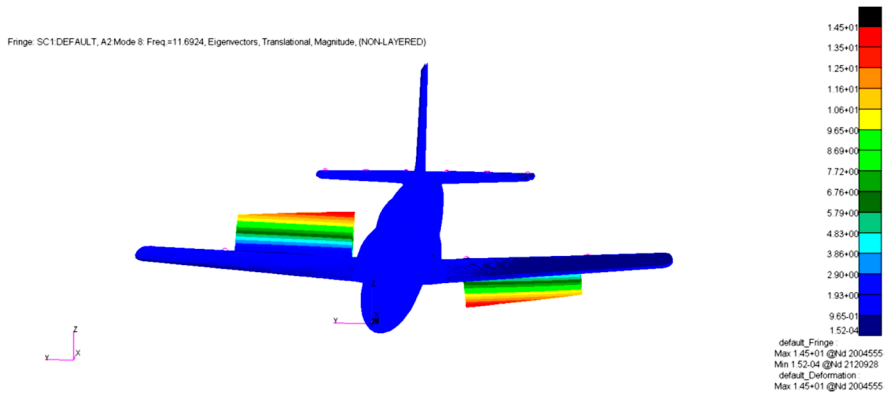


Figure 32. Antisymmetric flap rotation mode: f = 11.6924 Hz.

Figures 33–36 document the progression into global airframe dynamics and control surface interaction: symmetric wing bending at 16.4099 Hz, vertical tail bending at 18.2297 Hz, antisymmetric aileron rotation at 19.4495 Hz, and a coupled mode of wing bending with symmetric aileron rotation at 21.6891 Hz. This ordering is typical for a trapezoidal wing with a torsion box and hinged control surfaces and foreshadows the mode pairs that will dominate the V–g trends.

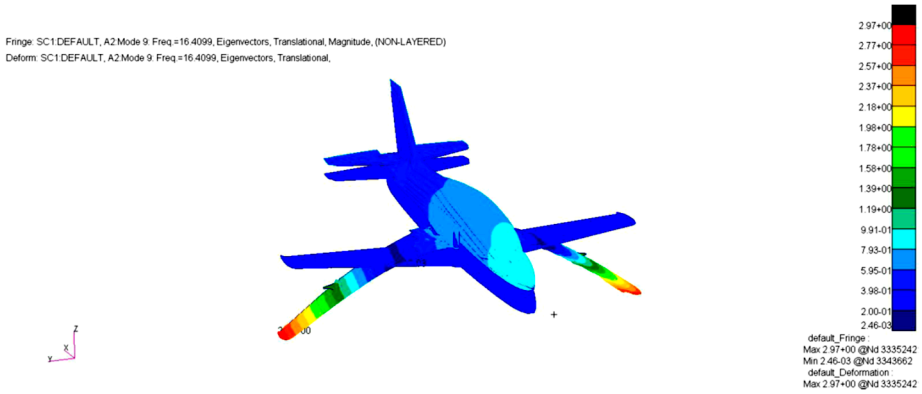


Figure 33. Symmetric wing bending mode: f = 16.4099 Hz.

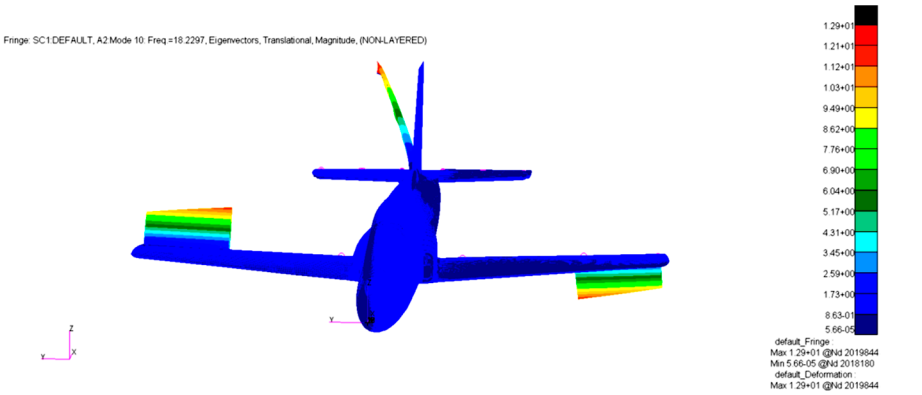


Figure 34. Vertical tail bending mode: f = 18.2297 Hz.

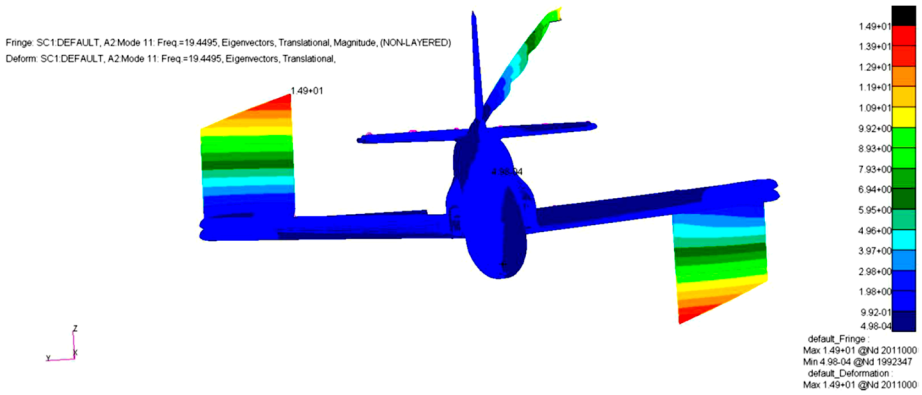


Figure 35. Antisymmetric aileron rotation mode: f = 19.4495 Hz.

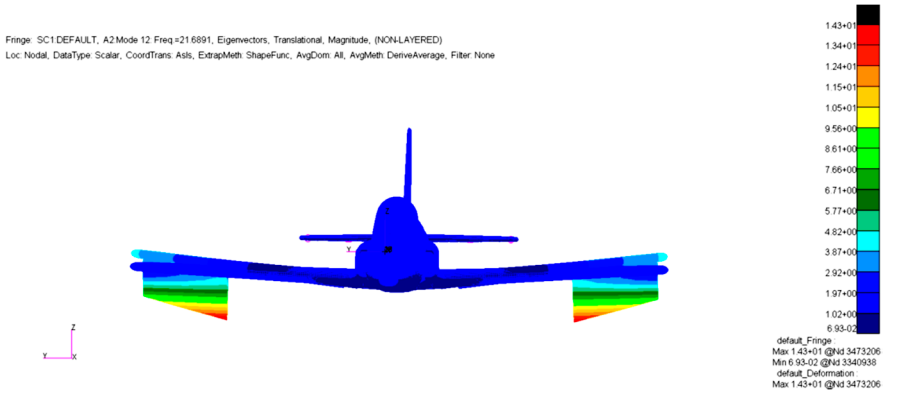


Figure 36. Wing bending with symmetric aileron rotation mode: f = 21.6891 Hz.

Finally, Figures 37–40 cover the empennage: antisymmetric horizontal tail bending at 37.2379 Hz, followed by elevator rotations—symmetric at 40.1101 Hz, antisymmetric at 43.1151 Hz, and another symmetric rotation at 47.5907 Hz. The steady increase in frequency from global bending to tail/control surface modes confirms a physically plausible modal hierarchy.

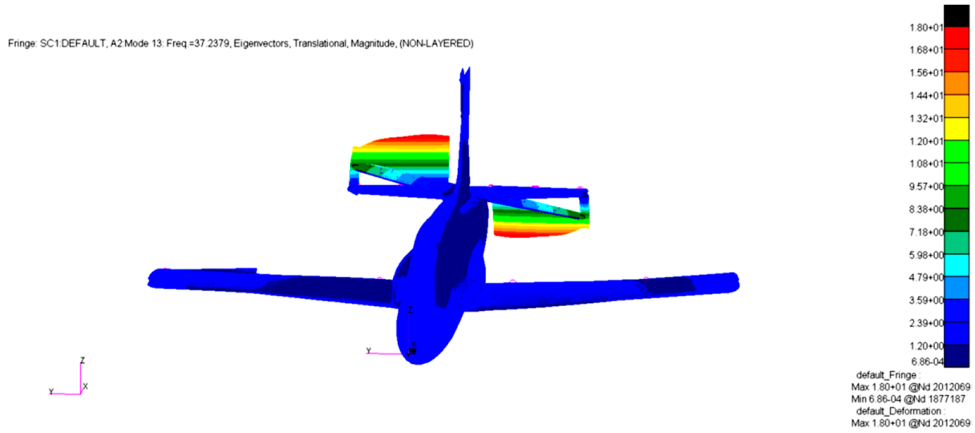


Figure 37. Antisymmetric horizontal tail bending mode: f = 37.2379 Hz.

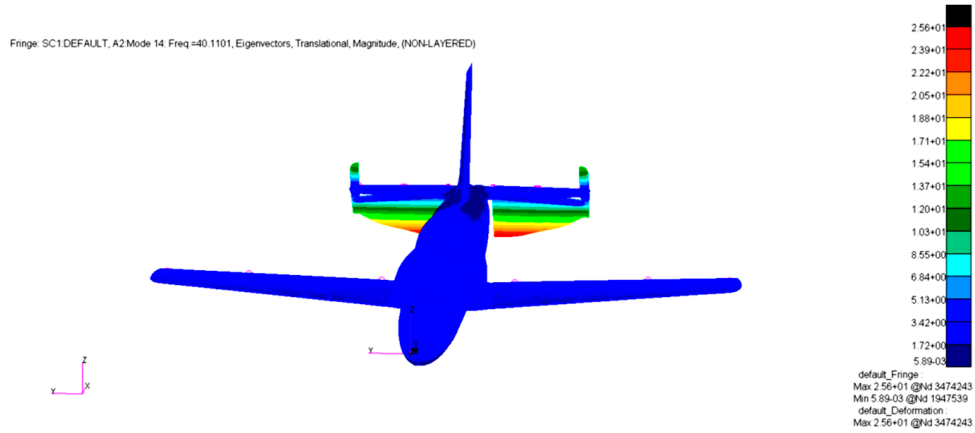


Figure 38. Symmetric elevator rotation mode: f = 40.1101 Hz.

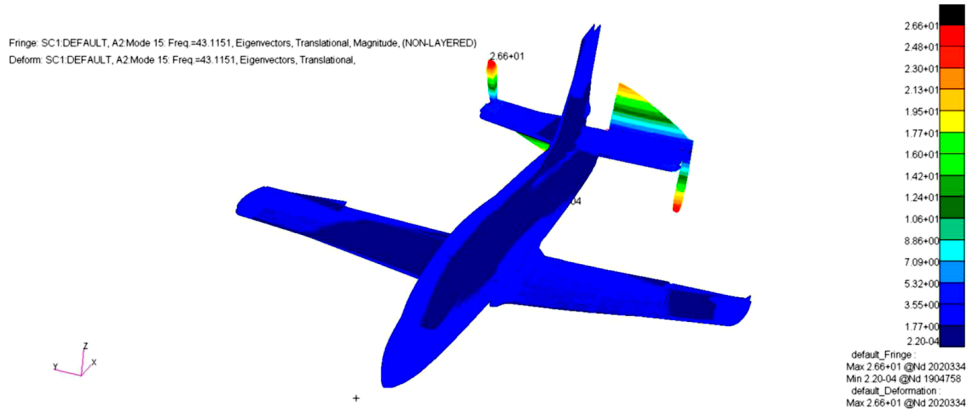


Figure 39. Antisymmetric elevator rotation mode: f = 43.1151 Hz.

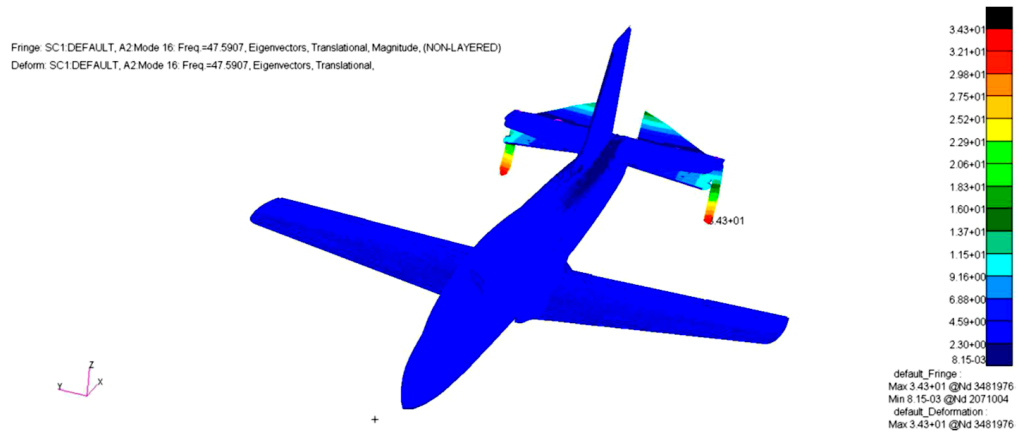


Figure 40. Symmetric elevator rotation mode: f = 47.5907 Hz.

Taken together, Figures 25–40 provide a coherent modal baseline: free–free rigid-body compliance, a realistic first elastic pair on the flaps, the expected wing/fin bending sequence, and the horizontal tail/elevator family at higher frequencies. This baseline underpins the DLM–FEM coupling and supports a reliable interpretation of the V–g curves and flutter mechanisms that follow in Section 3.

3.1.2. Flutter Analysis

The V–g curves were computed at four altitudes representative of the maneuver envelope (H = 0, 1500, 3000, and 5000 m), enabling us to track shifts in modal response and damping reserves against certification/operational limits, as shown in Figure 41.

Reading the altitude sweep of V–g curves (mode set 1–10) for the clean aircraft, the same pattern holds at H = 0, 1500, 3000, and 5000 m: all branches remain above g = 0 throughout the subsonic range, with the deepest damping minima occurring near the transonic end of the sweep (≈M 1.1–1.2) but never crossing the neutral line. We restrict the basis to the first ten elastic modes solely to avoid spectral crowding and keep the V–g/V–f loci interpretable, enabling reliable continuation and physical labeling of the unstable branch. The ordering of the branches mirrors the modal hierarchy identified for the clean model—flaps as the first elastic pair, followed by wing bending, vertical tail bending, aileron modes, then horizontal tail/elevator—and the most adverse trend is governed by the wing-bending family weakly coupled to control surface rotations at higher speeds. Altitude primarily shifts the level of aerodynamic damping without changing the active mechanism: lower air density at higher H slightly reduces damping margins, yet the curves stay positive across the entire subsonic domain. Extrapolating the most critical branch indicates a flutter onset beyond the subsonic regime, so a binary-mode interpretation (one excited/one exciting mode) is sufficient for safety assessment here. Together, these results confirm that the DLM–FEM clean model is flutter-free in subsonic and provide a robust baseline for comparing the effects of external store configurations.

V–g plots are shown versus Mach number (x-axis) with dimensionless modal damping g (y-axis; $g > 0$ stable, $g = 0$ flutter boundary); the legend identifies the modes, and an inset zooms the critical minima near $M \approx 0.8$.

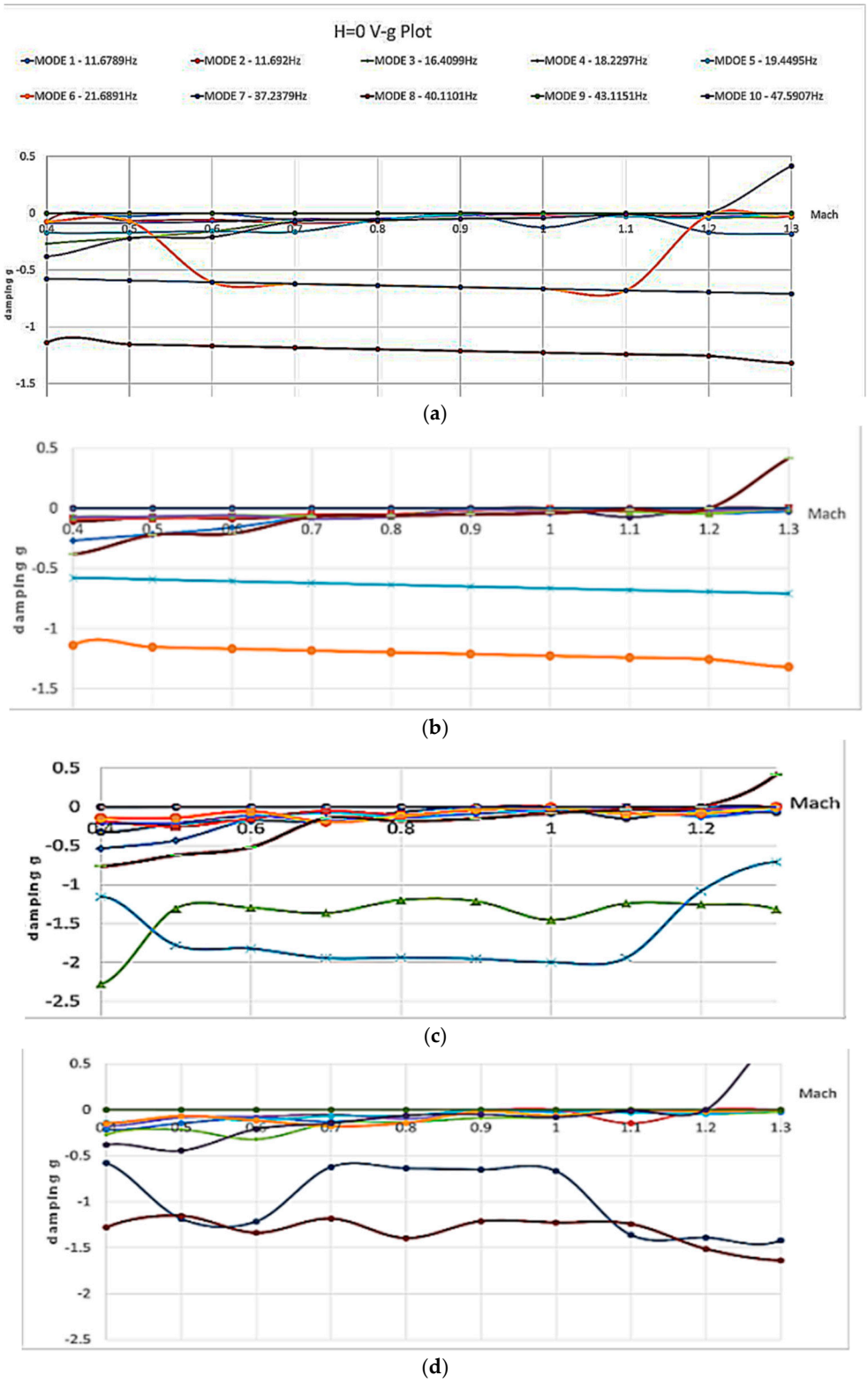


Figure 41. V–g curves at (**a**) H = 0 m, (**b**) H = 1500 m, (**c**) H = 3000 m and (**d**) H = 5000 m, for the mode combination 1–10.

3.2. Results for Four New Configurations

3.2.1. Modal Characteristics (A–D Configurations FEM)

In order to assess the aeroelastic stability margin, modal analysis provides the baseline frequencies and mode shapes of the loaded aircraft. The four external store layouts configuration (A–D) significantly affect both the global bending/torsional modes of the structure

and the local motions of the control surfaces and attached stores. Beyond the numerical values, the interpretation of these changes is essential to understand potential coupling scenarios that may lead to flutter or other aeroelastic instabilities.

Configuration A. This configuration represents a mixed load, with heavy inboard fuel tanks and lighter outboard launchers. The free–free rigid-body set occurs near zero frequency, confirming the unconstrained model. The first elastic family is given by the antisymmetric flap rotation at ~11.6 Hz, well separated from other modes. The global wing-bending mode appears at 15.9 Hz, followed by vertical tail bending around 18 Hz, which are typical baseline values.

The most distinctive feature of this layout is the presence of store-driven modes between 4.7 and 7.3 Hz, associated with launcher yaw and pitch oscillations. These low-frequency store motions are important because they may couple with atmospheric turbulence or pilot inputs. At higher frequencies (35–47 Hz), the empennage bending and elevator modes remain isolated and unaffected. Overall, Configuration A produces a balanced modal spectrum with sufficient separation between structural and store-driven modes, indicating relatively low aeroelastic risk.

Configuration B. With four heavy bombs, this configuration introduces a more compact and symmetric mass distribution. The effect is a slight increase in the wing-bending frequency to 16.3 Hz, which can be interpreted as an apparent stiffening due to mass concentration closer to the wing root. The flap and vertical tail families remain stable at ~11.7 Hz and ~18.2 Hz, respectively.

The modal signature is dominated by clear store pairs: yaw of outboard bombs at ~5.5 Hz, yaw of inboard bombs at ~6.2 Hz, and pitch/roll modes between 18 and 21 Hz. The aileron family, at 19.3–21.2 Hz, lies close to these store oscillations, suggesting potential localized coupling. However, the pairing symmetry keeps the spectrum orderly, with well-defined and separated groups.

Thus, Configuration B exhibits a structured modal response: store pairs are neatly clustered and relatively well isolated from primary wing and tail modes. This makes it one of the more "predictable" cases, and less prone to unpredictable coupling.

Configuration C. Distributing eight medium bombs across the wing makes Configuration C the most critical case. The wing-bending frequency drops significantly to 14.0 Hz (-12% compared with Configuration A), indicating a reduction in effective structural stiffness under dynamic loads.

This layout generates a very dense modal spectrum between 11.6 and 21.5 Hz. At low frequencies (4.3–5.4 Hz), bomb pitch modes dominate, while at ~11.7 Hz, an outboard bomb yaw mode overlaps closely with the flap family. More importantly, between 15.8 and 17.1 Hz, multiple store oscillations occur (yaw, pitch, symmetric and antisymmetric), in exactly the same band as the aileron modes (17.4–17.7 Hz).

This overlap between store and aileron modes represents the most unfavorable scenario observed: the likelihood of flutter or strong dynamic coupling is maximized. In conclusion, Configuration C provides the densest and most critical modal environment, with reduced structural frequencies and dangerous proximity between control surface and store modes.

Configuration D. This hybrid configuration combines the effect of inboard bombs with high-capacity outboard launchers. The wing-bending mode stabilizes at 15.5 Hz, close to the baseline, while the vertical tail remains at ~18 Hz.

At low frequency, store pitch modes appear again (5–7 Hz). A compact cluster of bomb roll and yaw modes develops between 16.5 and 16.9 Hz, comparable to Configuration C but less dense. The distinctive feature of this case is the presence of a launcher yaw doublet at

~29.8 Hz, which is absent from other layouts. This "signature" mode family could become relevant in supersonic regimes or under selective excitations.

In summary, Configuration D shows a mixed character: it retains wing and tail frequencies close to the baseline but introduces both a 16–17 Hz bomb cluster (with a risk of coupling) and a unique high-frequency launcher family at 29.8 Hz.

Detailed Comparative Analysis between Configurations A–D

Wing bending (first symmetric mode)

Frequencies range between 14.01 Hz (C) and 16.31 Hz (B). Configuration B, with four concentrated B-250 bombs, raises the wing-bending frequency to 16.31 Hz, suggesting an apparent stiffening of the global wing response due to the compact placement of mass close to the wing root, which favors the inertia distribution. Configuration C, with eight B-100 bombs distributed along the wing, strongly reduces the frequency to 14.01 Hz (−12%), indicating a decrease in effective dynamic stiffness and a tendency of the wing to deform more easily under dynamic loads. Configuration D restores the frequency to 15.54 Hz, close to reference case A, showing that the effects of the outboard launchers (PRN 32 × 42) and inboard bombs partially compensate each other. The conclusion is that the distribution of mass along the span is more critical than the total mass itself: distributed stores (C) reduce dynamic resistance, while concentrated stores (Configuration B) can even reinforce the wing response.

Vertical tail bending

The values are very close, between 17.6 and 18.2 Hz. Configuration C (17.63 Hz) shows a slight reduction, suggesting mild sensitivity to distributed wing masses, but overall the vertical tail remains stable and relatively insensitive to configurational changes.

Flaps

All configurations maintain flap frequencies in the 11.59–11.68 Hz range, with variations under 1%. This consistency confirms that the flaps, being located near the trailing edge and well supported structurally, are not significantly affected by external masses. Practically, this reduces the risk of interaction with store-driven modes in this band.

Aileron (first mode)

The aileron shows significant differences: from 20.46 Hz (A) down to 19.34 Hz (B, −5.5%) and 17.47 Hz (C, −14.6%). Configuration C, with eight distributed bombs, lowers the aileron frequency considerably, placing it in close proximity to the store cluster (~16–17 Hz). This proximity increases the likelihood of dynamic coupling and thus the risk of flutter or other unfavorable interactions under low-frequency excitations. Configuration B, although lowering the aileron frequency, still keeps it reasonably separated from the bomb modes (18–21 Hz). Configuration D does not explicitly list an aileron mode in this band, but the bomb cluster (16–17 Hz) plays a similar role in interacting with the structure.

Elevator

Frequencies range between 39.3 Hz (C) and 40.3 Hz (A). The differences are small, at about 2–3%, showing that the horizontal tail is only weakly influenced by the external configuration. However, Configuration C has the lowest value, which, combined with the marked reduction of wing and aileron frequencies, indicates a general trend of "softening" of the structure under distributed loads.

Store-specific families:

In the 4–7 Hz range, all configurations show mass-induced modes (tanks, bombs, launchers). These are critical because they represent rigid-body-like motions of the stores, with potential interaction under external excitations (turbulence, abrupt maneuvers).

In the ~11.6–11.8 Hz range, only Configuration C exhibits an outboard bomb yaw mode, very close to the flap modes. This local coincidence suggests a potential interaction zone that requires attention in flutter analysis.

In the ~16–17.5 Hz range, the highest mode density is observed: Configuration C has multiple store vibrations (inboard/outboard, yaw/pitch), overlapping with the aileron modes, creating a highly coupling-prone environment. Configuration D also has a bomb cluster in the same band, but cleaner. Configuration B shows bomb modes at slightly higher values (~18–21 Hz), that are thus better separated from the aileron. A has fewer store modes in this range, resulting in a more "open" spectrum.

At ~29.8 Hz, only Configuration D introduces a clear launcher doublet, distinct from the rest of the spectrum. This could become a unique signature of this configuration, especially at frequencies close to the natural vibrations of the wing–structural profile assembly.

Comparative analysis shows that the distribution of stores along the wing span has a much greater impact on the modal spectrum than the total mass. Configuration C (8× B-100 distributed) is the most critical, significantly lowering global modal frequencies and overlapping the aileron modes with store modes, which increases the risk of aeroelastic instabilities. Configuration B (4× B-250 concentrated) produces a more orderly spectrum, with clear separation between structural and store modes, making it the "safest" of the four. Configuration D has a hybrid behavior: it keeps wing and tail values close to the reference, but introduces distinct clusters (16–17 Hz for bombs, 29.8 Hz for launchers) that may generate selective resonances. Configuration A remains intermediate, with a balanced spectrum and no critical overlaps.

3.2.2. Flutter Analysis for A–D Configurations

This section reviews the V–g curves for the four external store configurations (A–D) of the IAR-99 Șoim, grouped by representative altitudes of the maneuver envelope: H = 0, 1500, 3000, and 5000 m. For each case, the p-k method uses ~9–10 elastic modes (Figures 42–45).

For H = 0 m, Configuration A, the V–g bundle shows no subsonic flutter. The governing pair is a control surface rotation (excited) weakly coupled with a tail/wing bending branch (exciting). The g = 0 crossing lies near M ≈ 1.2, i.e., outside the subsonic range. Configuration B shows similar behavior: the most adverse trend still extrapolates to a g = 0 crossing near M ≈ 1.2. The dominant interaction involves symmetric wing bending coupled with store pitch/roll on the outer stations. Configuration C is the most critical sea level case. A store-driven antisymmetric family couples with a symmetric store motion on the outboard stations, producing a subsonic g = 0 crossing around M ≈ 0.82. Configuration D is also critical at sea level: a tail-bending family coupled with symmetric store roll yields a subsonic crossing near M ≈ 0.82.

At H = 1500 m, the modal ordering mirrors sea level and the lower dynamic pressure mainly shifts damping upward. Configuration A and B show smooth, well-separated branches with ample margin across the subsonic range. In Configuration C, the multi-store layout produces mode crowding: two store-driven branches develop pronounced dips (around the mid–high subsonic region), approach the neutral line, then recover—so the tightest margins occur near transonic onset but remain positive. Configuration D exhibits a similarly busy, oscillatory bundle due to the mixed inboard-rack/outboard-launcher interference; several branches trade dominance between roughly M ≈ 0.9–1.2, with a narrow minimum near the high-subsonic end, yet no crossing of g = 0. The net effect is that altitude eases the sea level criticality of Configuration C and D without introducing new governing mechanisms.

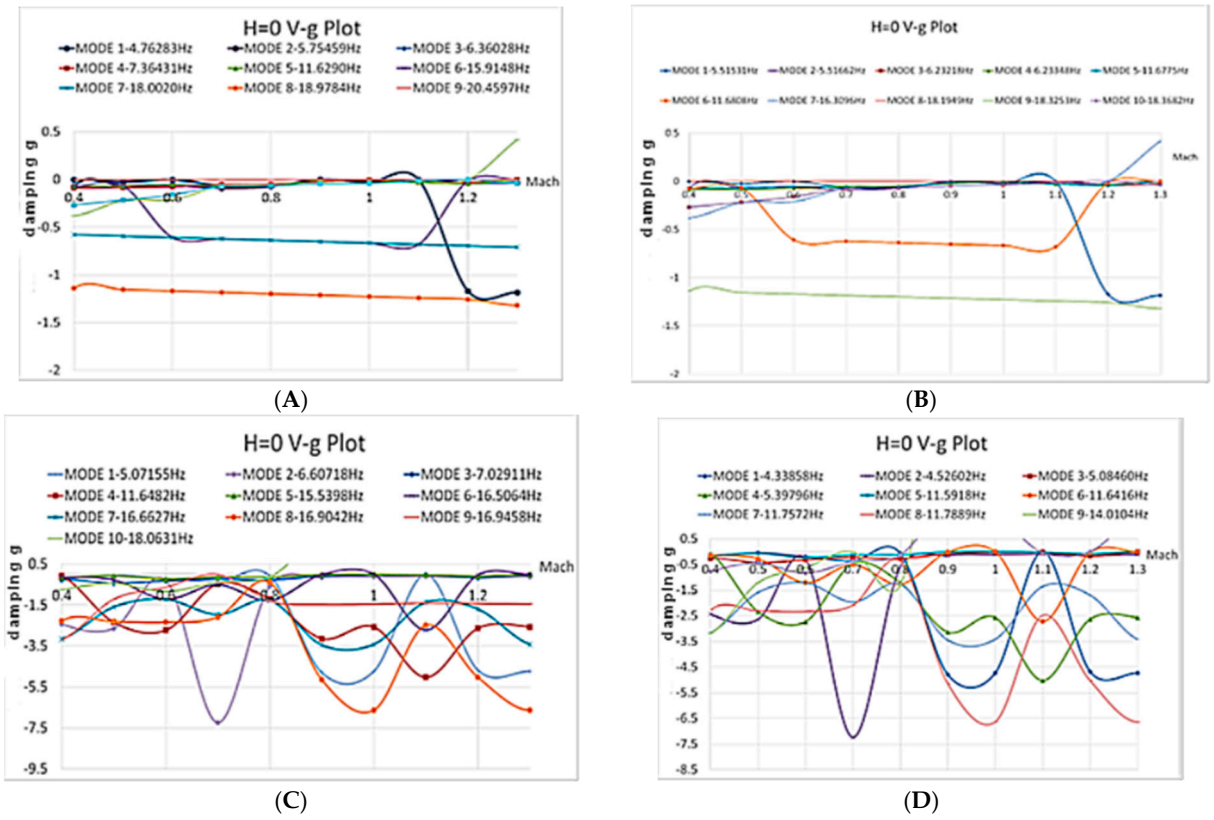


Figure 42. V–g curves at H = 0 m for the four configurations (**A**–**D**), mode combination 1–10.

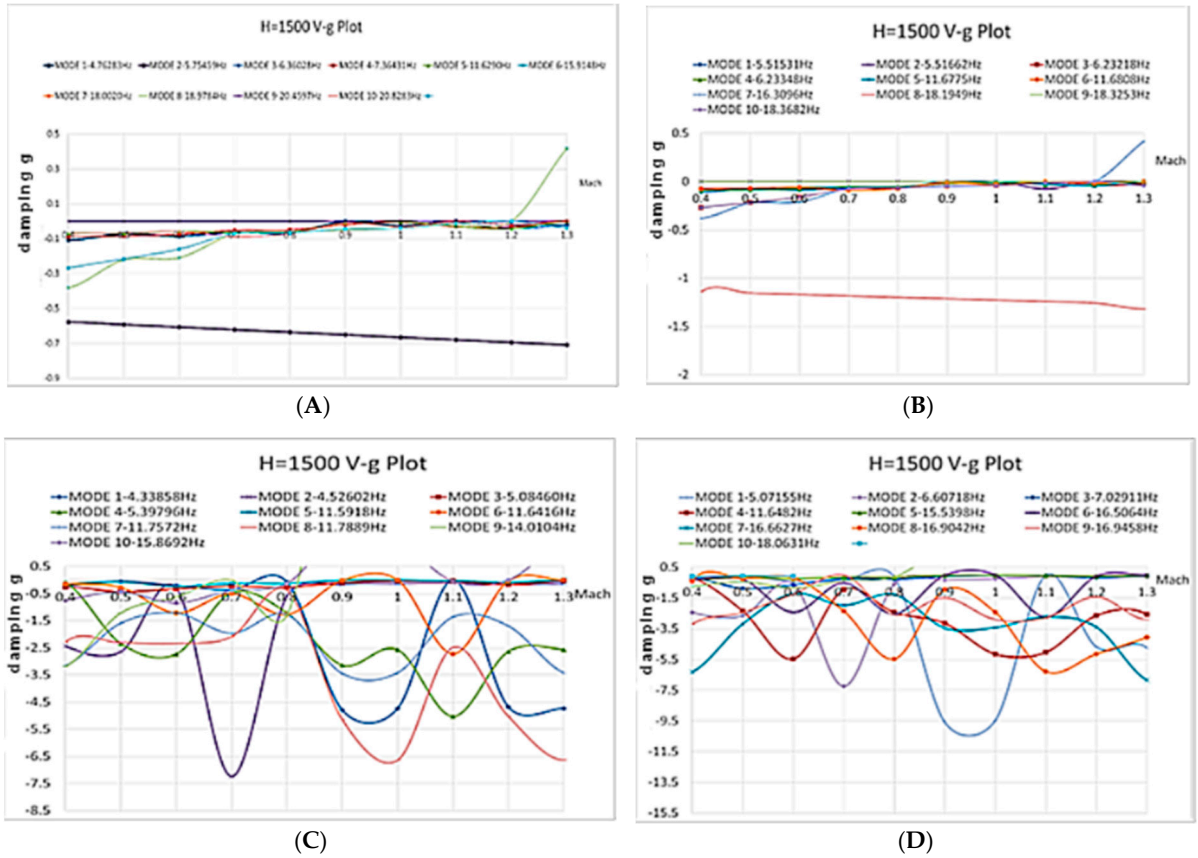


Figure 43. V–g curves at H = 1500 m for the four configurations (**A–D)**, mode combination 1–10.

At H = 3000 m, the behavior remains consistent with the lower altitudes, but the reduced dynamic pressure shifts the critical features to slightly higher Mach and softens the deepest minima. Configuration A and B show no subsonic g = 0 crossings; their bundles are smooth, with the wing-bending-dominated branch dipping near the high-subsonic region and then recovering. In Configuration C, the multi-store layout again produces mode crowding and two pronounced troughs, yet both minima are displaced to higher Mach and stay above the neutral line, indicating improved margin versus sea level. Configuration D exhibits an equally busy, oscillatory bundle caused by the mixed inboard-rack/outboard-launcher interference; several branches trade dominance between about M ≈ 0.9–1.2, but the worst dip also shifts right and remains positive. Overall, altitude pushes any potential crossing to higher speeds: configurations Configuration C and D still define the tightest margins, while Configuration A and B retain comfortable subsonic damping.

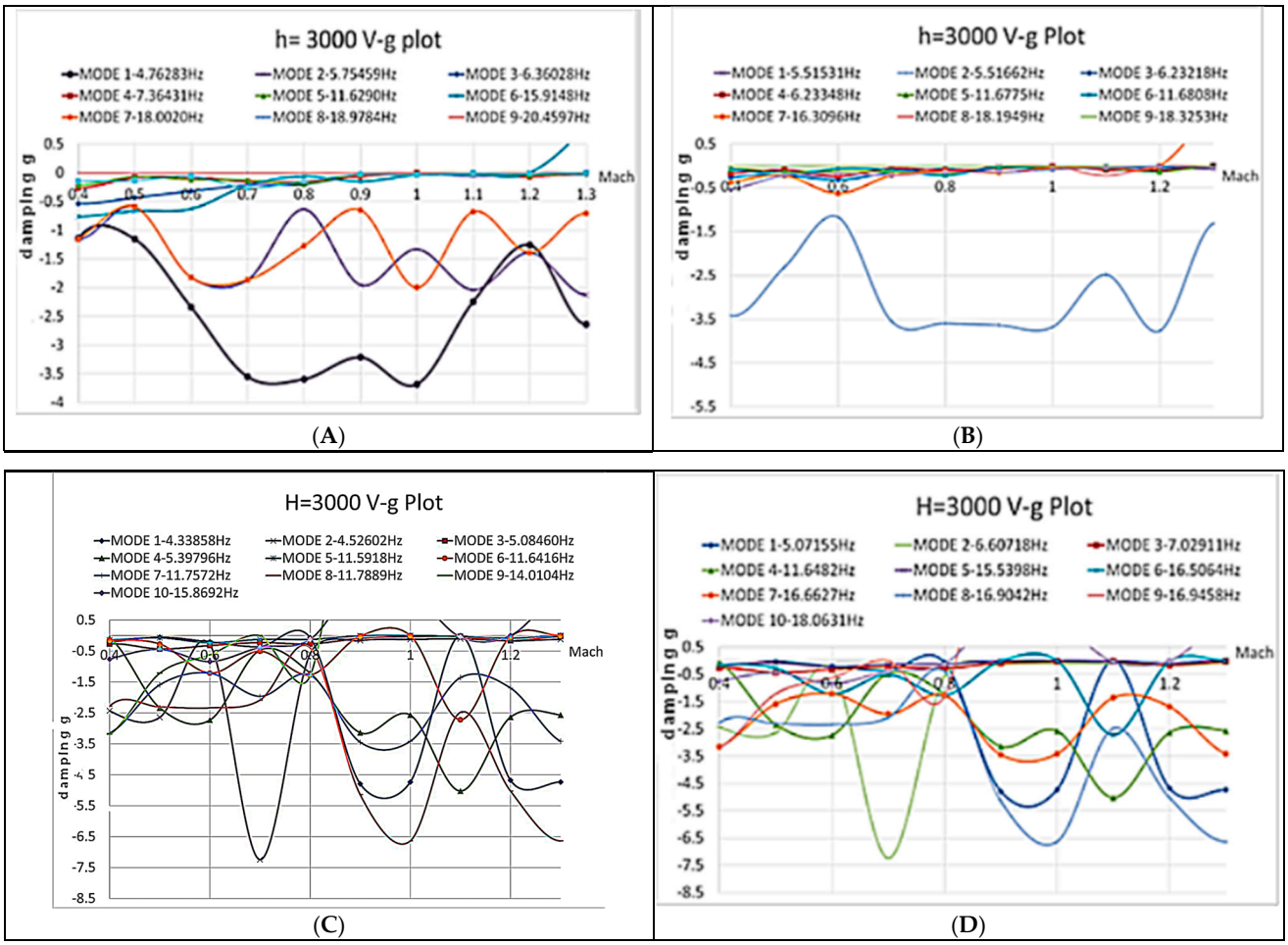


Figure 44. V–g curves at H = 3000 m for the four configurations (**A**–**D**), mode combination 1–10.

At H = 5000 m, the reduced dynamic pressure lifts the entire V–g bundles and shifts the deepest minima to higher Mach. Configuration A shows smooth, small-amplitude oscillations with a gentle dip toward the high-subsonic end that stays above the neutral line. Configuration B is similarly well behaved: one dominant, wavy branch varies with Mach but never approaches g = 0. In Configuration C, the multi-store layout still produces several pronounced troughs (mode crowding), yet the worst minima are displaced to around M ≈ 1.0–1.2 and remain positive—an improvement over lower altitudes. Configuration D retains a busy, oscillatory signature due to the mixed inboard-rack/outboard-launcher interference; the deepest dip also shifts right and recovers before transonic onset. Overall, the ordering of dominant modes is unchanged, and all configurations remain flutter-free

in subsonic, and although Configuration C and D continue to define the tightest margins, their damping at 5000 m is less critical than at sea level.

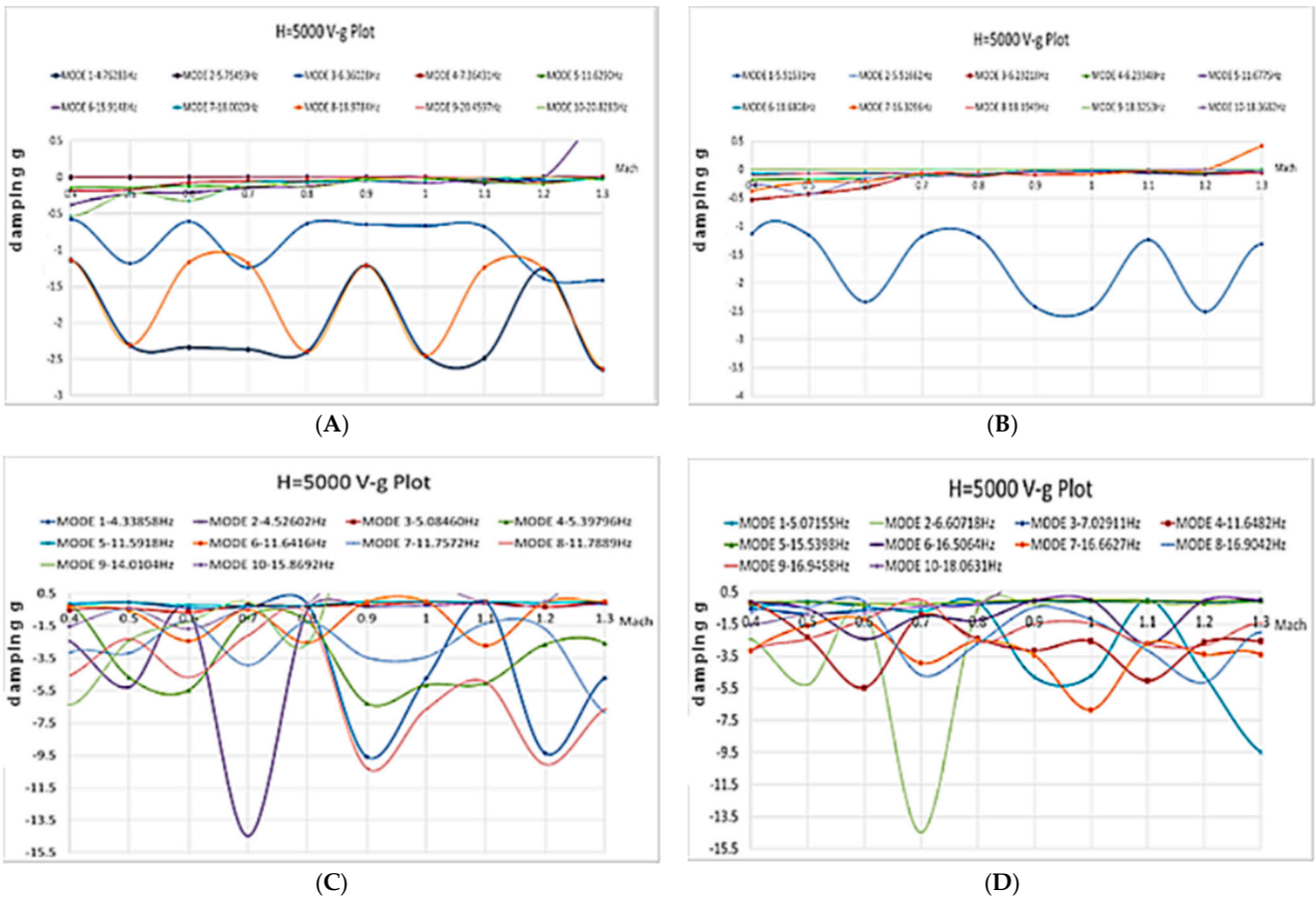


Figure 45. V–g curves at H = 5000 m for the four configurations (**A**–**D**), mode combination 1–10.

Altitude-wise synthesis

Configuration A and B: adequate subsonic damping margins at all altitudes; any predicted flutter lies in supersonic, outside the subsonic operating domain.

Configuration C and D: subsonic critical pairs at H = 0 m (≈M 0.82) with the same mechanisms persisting with altitude; these define the sensitivity envelope and point to possible mitigations (mass distribution, pylon–store stiffening, etc.).

Overall, the clean-to-stores methodology captures store-specific mode families and preserves credible load paths via the DLM over FEM coverage, yielding consistent p-k results across altitudes for all four configurations.

The results obtained in this study highlight several important insights regarding the aeroelastic behavior of the IAR-99 aircraft when equipped with external stores. A first critical observation is that the distribution of mass along the wing span exerts a stronger influence on the modal spectrum than the absolute total mass. While the heavy and compact load of Configuration B (4× B-250 bombs) increased the wing-bending frequency and produced a relatively orderly spectrum, the distributed load of Configuration C (8× B-100 bombs) led to a significant reduction in structural frequencies and created a dense modal environment with high coupling potential. This demonstrates that spanwise positioning of external stores is a governing parameter in defining aeroelastic margins.

Another key finding is that store-induced rigid-body modes in the 4–7 Hz range are consistently present across all configurations. These modes are not captured in clean aircraft analyses and represent new families of potential interactions, particularly with

atmospheric turbulence and maneuver excitations. The identification of these families shows the necessity of explicitly incorporating store models into aeroelastic assessments rather than relying solely on clean configurations.

From a methodological standpoint, the study provides a validated FEM–DLM coupling framework for a complete trainer aircraft configuration, which had not been systematically reported in the literature. Previous works mainly focused on fighters, UAVs, or simplified wing–store systems, while trainer aircraft such as the IAR-99 remained underrepresented. The present work fills this gap by offering a high-fidelity structural model, fully integrated with pylon–store attachments, and consistent aerodynamic coverage. This combination ensures that both local store dynamics and global structural responses are faithfully represented in the flutter predictions.

In terms of novelty, this research shows for the first time that certain configurations (C and D) can generate subsonic critical flutter pairs near Mach 0.82 at sea level, whereas others (Configuration A and B) remain stable across the subsonic domain. This result has practical implications for flight certification: it points to specific payload layouts that should be restricted or require design reinforcements (e.g., stiffer pylons, dampers, or store modifications). Moreover, the identification of a unique launcher signature at ~29.8 Hz in Configuration D represents a distinctive contribution, as it provides a diagnostic marker for launcher-equipped configurations in modal testing and operational monitoring.

The utility of the study is twofold:

For certification authorities, it provides a structured methodology to evaluate the aeroelastic impact of multiple external stores on a light military trainer, supporting safe operational envelope definition.

For the design and modernization of the IAR-99 platform (and similar aircraft), the results inform decisions on optimal store placement, highlight critical configurations to avoid, and suggest potential mitigation strategies to extend operational flexibility without compromising flutter margins.

In summary, the contributions of this work consist of:

Extending FEM–DLM aeroelastic methodologies to a complete trainer aircraft with multiple store configurations.

Demonstrating that mass distribution along the span is more critical than total mass in determining flutter susceptibility.

Identifying new families of store-driven low-frequency modes and their interaction potential.

Revealing specific critical configurations (C and D) that can induce subsonic flutter onset.

Providing a validated computational framework and reference database that can be directly applied to certification and modernization of the IAR-99 HAWK.

4. Conclusions

This study developed and validated a new FEM–DLM aeroelastic coupling methodology applied to the IAR-99 HAWK trainer aircraft carrying external stores. The main conclusions are:

Mass distribution governs aeroelastic margins. The spanwise placement of stores influences natural frequencies more strongly than total payload mass. Concentrated heavy bombs (Configuration B) stiffen the response, while distributed medium bombs (Configuration C) soften the structure and reduce modal separation.

New families of store-driven modes were identified. Across all configurations, rigid-body-like oscillations in the 4–7 Hz band appear, which are absent in clean aircraft analyses. These modes can couple with atmospheric turbulence or pilot inputs and must be explicitly considered in flutter assessments.

Critical subsonic flutter was found in certain layouts. Configurations C and D exhibited flutter onset near Mach 0.82 at sea level, whereas Configurations A and B remained flutter-free in the subsonic range. These results provide actionable guidance for payload restrictions and structural reinforcements in certification campaigns.

A launcher-specific modal signature was discovered. Configuration D introduced a unique high-frequency launcher family at ~29.8 Hz, which was absent in other cases. This marker can be used for experimental validation and monitoring of launcher-equipped aircraft.

Methodological contribution: The validated FEM–DLM framework extends aeroelastic methodologies to trainer aircraft, providing a transferable approach that captures both local store dynamics and global structural responses.

Overall, the study closes a literature gap by addressing flutter of trainer-class aircraft with external stores, highlights critical configurations with subsonic instabilities, and provides a validated computational methodology with direct utility for certification and modernization of the IAR-99 HAWK and similar platforms.

Author Contributions: Conceptualization, G.C. and I.F.; methodology, T.V. and T.V.J.; software, T.V.J.; validation, T.V.; writing—original draft preparation, G.C., I.F., T.V. and T.V.J.; writing—review and editing, G.C., I.F., T.V. and T.V.J.; visualization, T.V.; supervision I.F. All authors have read and agreed to the published version of the manuscript.

Funding: This work was funded by The National University of Science and Technology POLITEHNICA Bucharest through the PubArt programme.

Data Availability Statement: The original contributions presented in this study are included in the article, further inquiries can be directed to the corresponding author.

Conflicts of Interest: Authors T.V. and T.V.J. were employed by the company 3 Black Business Solutions Srl. The remaining authors declare that the research was conducted in the absence of any commercial or financial relationships that could be construed as a potential conflict of interest.

References

1. Bisplingboff, R.L.; Ashley, H.; Halfman, R.L. *Aeroelasticity*; Addison-Wesley Publishing Company: Cambridge, MA, USA, 1955.
2. Čečrdle, J. 1—Introduction to aircraft aeroelasticity and whirl flutter. In *Whirl Flutter of Turboprop Aircraft Structures*; Woodhead Publishing: Sawston, UK, 2015; pp. 1–12. [CrossRef]
3. Available online: https://www.intertekinform.com/en-us/standards/mil-a-8870-revision-c-1993-690098_saig_mil_mil_1591500/ (accessed on 1 July 2025).
4. Available online: https://www.easa.europa.eu/en/document-library/certification-specifications/group/cs-23-normal-utility-aerobatic-and-commuter-aeroplanes (accessed on 1 July 2025).
5. Moosavi, M.R.; Oskouei, A.R.N.; Khelil, A. Flutter of subsonic wing. *Thin-Walled Struct.* **2005**, *43*, 617–627. [CrossRef]
6. Voss, G.; Schaefer, D.; Vidy, C. Investigation on flutter stability of the DLR-F19/SACCON configuration. *Aerosp. Sci. Technol.* **2019**, *93*, 105320. [CrossRef]
7. Mozaffari-Jovin, S.; Firouz-Abadi, R.D.; Roshanian, J. Flutter of wings involving a locally distributed flexible control surface. *J. Sound Vib.* **2015**, *357*, 377–408. [CrossRef]
8. Silva, G.C.; Donadon, M.V.; Silvestre, F.J. Experimental and numerical investigations on the nonlinear aeroelastic behavior of high aspect-ratio wings for different chord-wise store positions under stall and follower aerodynamic load models. *Int. J. Non-Linear Mech.* **2021**, *131*, 103685. [CrossRef]
9. Pike, E.C. *AGARD Report No. 578 Manual on Aeroelasticity*; Technical Editing and Reproduction Ltd.: London, UK, 1971.
10. Peters, N.; Wissink, A.; Ekaterinaris, J. Machine learning-based surrogate modeling approaches for fixed-wing store separation. *Aerosp. Sci. Technol.* **2023**, *133*, 108150. [CrossRef]
11. Cakmak, E.; Kurnaz, M.; Kilic, D.; Nikbay, M. CFD-Based Techniques for Flutter Prediction Through the Generation of Generalized Aerodynamic Forces. In Proceedings of the AIAA 2025-3294 Session: Applied Aeroelasticity and Fluid-Structure Interaction, Las Vegas, NV, USA, 16 July 2025. [CrossRef]
12. Ang, E.H.W.; Ng, B.F. Stability Analysis of Body-Freedom Flutter in Flying Wing Unmanned Aerial Vehicles. *AIAA J.* **2025**, 1–9. [CrossRef]

13. Xu, Q.; Hou, L.; Ren, S.; Hou, L.; Li, Z.; Saeed, N.A. Flutter Analysis of a 2.5D C/SiC Composite Blade Considering Wake Excitation. *J. Vib. Eng. Technol.* **2025**, *13*, 367. [CrossRef]
14. Kim, H.; Kim, M.; Shin, B.; Jo, Y. A Study on the Flight Safety Analysis of Military Aircraft External Stores. *J. Korean Mil. Sci. Technol. Soc.* **2023**, *26*, 83–90. [CrossRef]
15. Yuet, S.K.; Imisi-Oluwa, A.; Mat, S. Experimental Investigation of a Generic Light Aircraft Model with Dual External Stores. In *Proceedings of the 2nd International Seminar on Aeronautics and Energy (ISAE 2022), Virtual, 17 September 2022*; Lecture Notes in Mechanical Engineering; Nik Mohd., N.A.R., Mat, S., Eds.; Springer: Singapore, 2024. [CrossRef]
16. Gade, P.V.N.; Inman, D.J. $\mathcal{H}_\infty$ Controller Design for Wing/Store Flutter Suppression. In Proceedings of the ASME 1996 International Mechanical Engineering Congress and Exposition. Active Control of Vibration and Noise, Atlanta, GA, USA, 17–22 November 1996; ASME: New York, NY, USA; pp. 91–99. [CrossRef]
17. Abou-Kebeh, S.; Gil-Pita, R.; Rosa-Zurera, M. Application of Deep Learning to Identify Flutter Flight Testing Signals Parameters and Analysis of Real F-18 Flutter Flight Test Data. *Aerospace* **2025**, *12*, 34. [CrossRef]
18. Kwon, J.; Yoo, J.H.; Lee, I. Effects of Structural Damage and External Stores on Transonic Flutter Stability. *Int. J. Aeronaut. Space Sci.* **2018**, *19*, 636–644. [CrossRef]
19. Kang, L.H.; Lee, S.J.; Lee, I.; Han, J.H. Flutter Characteristics and Active Vibration Control of Aircraft Wing with External Store. *J. KIMS Technol.* **2007**, *10*, 73–80.
20. Hoq, K.M.T.; Talal, A.; Mat, S.; Ramli, Y. Effect of External Store on a Generic Subsonic Fighter Aircraft. *J. Aeronaut. Astronaut. Aviat.* **2024**, *56*, 1069–1080. [CrossRef]
21. Zheng, Y.; Wang, Y. Flutter stability analysis of aeroelastic systems with consideration of hybrid uncertain parameters. *Mech. Syst. Signal Process.* **2023**, *185*, 109782. [CrossRef]
22. Vindigni, C.R.; Mantegna, G.; Orlando, C.; Alaimo, A.; Berci, M. A refined aeroelastic beam finite element for the stability analysis of flexible subsonic wings. *Comput. Struct.* **2025**, *307*, 107618. [CrossRef]
23. Gern, F.H.; Librescu, L. Effects of externally mounted stores on aeroelasticity of advanced swept cantilevered aircraft wings. *Aerosp. Sci. Technol.* **1998**, *2*, 321–333. [CrossRef]
24. Fazelzadeh, S.A.; Ghasemi, A.H.; Mazidi, A. Aeroelastic Analysis of Unrestrained Aircraft Wing with External Stores Under Roll Maneuver. *Int. J. Acoust. Vib.* **2016**, *21*, 327333. [CrossRef]
25. Byun, K.-H.; Jun, S.-M. Flutter Analysis of F-16 Aircraft Utilizing Test Modal Data. In Proceedings of the 25th International Congress of the Aeronautical Sciences, Hamburg, Germany, 3–8 September 2006.
26. Amoozgar, M.; Shahverdi, H. Investigation of adding fins to external stores for improving the flutter characteristics of a wing/store configuration. *Proc. Inst. Mech. Eng. Part G J. Aerosp. Eng.* **2015**, *230*, 1507–1517. [CrossRef]
27. Lei, Y.; Ye, Z. The interference aerodynamics caused by the wing elasticity during store separation. *Acta Astronaut.* **2016**, *121*, 116–129. [CrossRef]
28. Jonsson, E.; Riso, C.; Lupp, C.A.; Cesnik, C.E.S.; Martins, J.R.R.A.; Epureanu, B.I. Flutter and post-flutter constraints in aircraft design optimization. *Prog. Aerosp. Sci.* **2019**, *109*, 100537. [CrossRef]
29. Available online: https://www.incas.ro/iar-99-and-successors-program/ (accessed on 1 July 2025).
30. Stefanescu, I. Utilization of simple and double control subsonic aircraft for advanced combat training of the military pilots. *INCAS Bull.* **2012**, *4*, 103–114. [CrossRef]
31. Catana, R.M.; Badea, G.P. Experimental Analysis on the Operating Line of Two Gas Turbine Engines by Testing with Different Exhaust Nozzle Geometries. *Energies* **2023**, *16*, 5627. [CrossRef]
32. Yuan, W.; Zhang, X. Numerical Stabilization for Flutter Analysis Procedure. *Aerospace* **2023**, *10*, 302. [CrossRef]
33. Böhnisch, N.; Braun, C.; Marzocca, P.; Muscarello, V. Impact of Aerodynamic Interactions on Aeroelastic Stability of Wing-Propeller Systems. *Appl. Sci.* **2024**, *14*, 8709. [CrossRef]
34. Yu, Q.; Damodaran, M.; Khoo, B.C. Predicting wing–pylon–nacelle configuration flutter based on finite element and aerodynamic panel methods. *Adv. Aerodyn.* **2023**, *5*, 52. [CrossRef]
35. Yuan, W. Rimple Sandhu and Dominique Poirel, Fully Coupled Aeroelastic Analyses of Wing Flutter towards Application to Complex Aircraft Configurations. *J. Aerosp. Eng.* **2020**, *34*, 2. [CrossRef]

Disclaimer/Publisher's Note: The statements, opinions and data contained in all publications are solely those of the individual author(s) and contributor(s) and not of MDPI and/or the editor(s). MDPI and/or the editor(s) disclaim responsibility for any injury to people or property resulting from any ideas, methods, instructions or products referred to in the content.